Heat Pump Design for Industrial Drying

A Design Study into the Optimisation and Sizing of an Industrial Heat Pump Dryer with Evaporator Bypass and Recirculation for a Non-Isenthalpic Drying Process

J. H. Lammers

Delft University of Technology

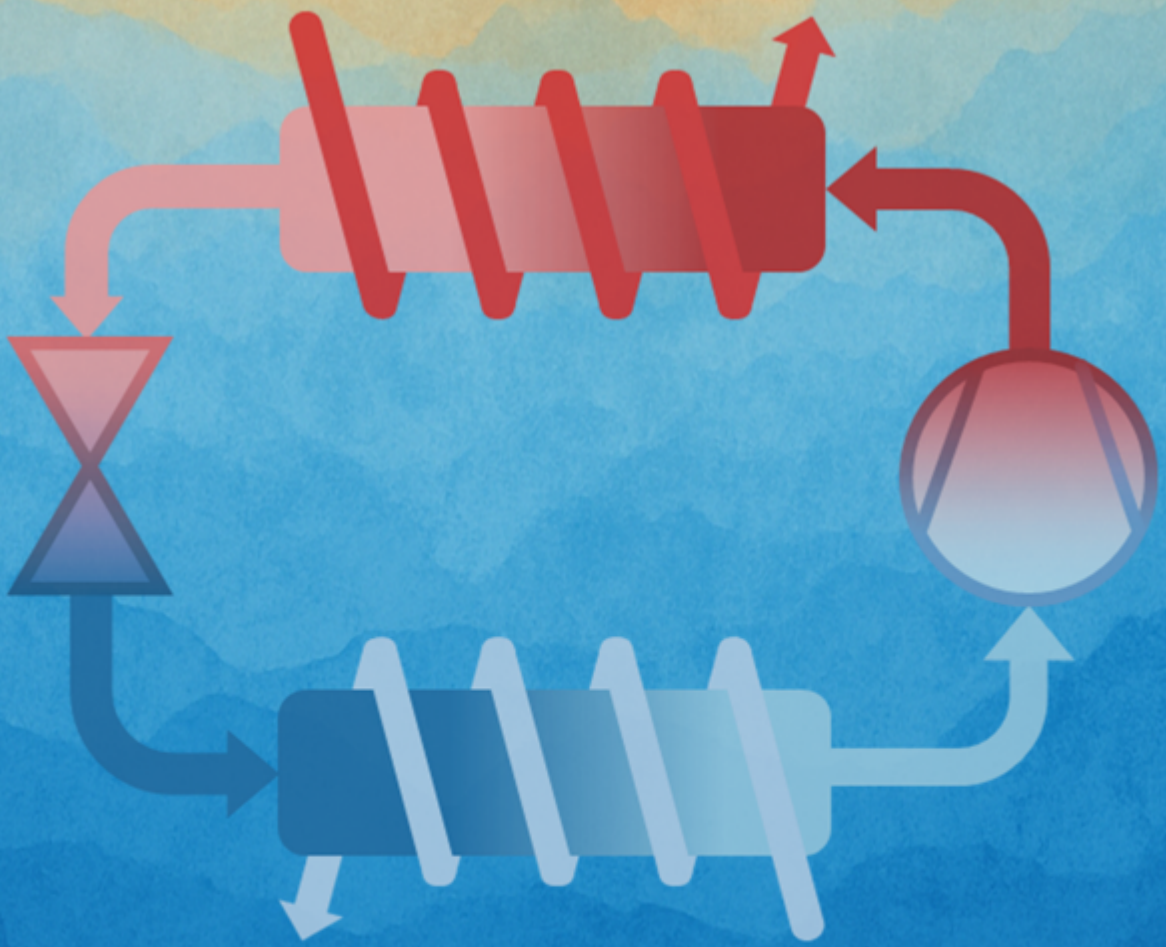

TU Delft

Heat Pump Design for Industrial Drying

A Design Study into the Optimisation and Sizing of an Industrial Heat Pump Dryer with Evaporator Bypass and Recirculation for a Non-Isenthalpic Drying Process

by

J. H. Lammers

to obtain the degree of Master of Science

at the Delft University of Technology,

to be defended publicly on Friday November 28, 2025 at 14:00.

Student number:	4799674	
Project duration:	January 1, 2025 – November 28, 2025	
Thesis committee:	Dr. ir. J. W. R. Peeters,	TU Delft, supervisor
	Prof. Dr. ir. S. A. Klein	TU Delft, supervisor
	Dr. E. Zanetti,	TU Delft

Style: TU Delft Report Style, with modifications by Daan Zwaneveld

An electronic version of this thesis is available at http://repository.tudelft.nl/.

TU Delft

Preface

I am pleased to present my thesis, ”Heat Pump Design for Industrial Drying: A Design Study into the Optimisation and Sizing of an Industrial Heat Pump Dryer with Evaporator Bypass and Recirculation for a Non-Isenthalpic Drying Process.” This thesis represents the final step in my Master’s program in Mechanical Engineering, specialising in Process, Flow, and Energy Technology at Delft University of Technology. This work was conducted between January and November 2025 at the Department of Process and Energy, focusing on the design, optimisation, and sizing of a high-temperature heat pump dryer with an evaporator bypass and air recirculation.

Working on this project has allowed me to combine my interests in thermodynamics, industrial energy systems, and sustainable technology. While identifying the optimal methods for enhancing the heat pump cycles presented challenges, it has been rewarding to see the results of my hard work.

I want to express my gratitude to my supervisors, Prof. Dr. Ir. Sikke Klein, Prof. Dr. Rene Pecnik, and Dr. Ir. Jurriaan Peeters. Your guidance, insightful feedback, and continuous support have been invaluable throughout this project. Collaborating with you to tackle the challenges I faced has greatly enriched my experience. I am genuinely appreciative of the insights you offered at every stage, and your mentorship has made a significant impact on my development. I look forward to applying everything I’ve learned!

Lastly, I want to thank my dear parents for always believing in me, encouraging me, and being proud of me. I also want to express my gratitude to my wonderful girlfriend for her unwavering support and for patiently listening to my thoughts and ideas. Her support has given me the excellent opportunity to practice explaining things in simple terms.

J. H. Lammers
Delft, November 2025

Abstract

Industrial drying processes are energy-intensive and account for a significant portion of energy consumption in the paper, food, and wood processing industries. As the goal of achieving net-zero emissions by 2050 gains importance, electrifying these processes with heat pumps emerges as a promising, innovative solution. This study investigates the optimal configuration of heat pumps, the selection of working fluids, and the sizing of components for a non-isenthalpic 530 kWth drying cycle that includes evaporator bypass and recirculation of the humid air.

Two heat pump configurations were analysed: a single-stage heat pump and a cascade heat pump. Both cycles were simulated and optimised using zeotropic mixtures of natural refrigerants, with molar compositions adjusted to minimise total entropy production. The compressors and heat exchangers were modelled and sized to facilitate a component-level comparison between the cycles.

The results indicate that using zeotropic mixtures improves the performance of both heat pump configurations. However, it is not always necessary to operate in transcritical mode for optimal performance. A single-stage heat pump cycle using a zeotropic mixture of 96 mol% isobutane and 4 mol% propylene exhibits the best performance, achieving a coefficient of performance (COP) of 2.54. In comparison, the best-performing cascade heat pump cycle has a COP that is 4.3% higher than that of the best single-stage heat pump cycle. However, due to its 91% larger total heat transfer area and the requirement for two compressors, the capital costs of the cascade system are significantly higher than those of the single-stage system.

In conclusion, the best option is a single-stage heat pump equipped with an internal heat exchanger, using a zeotropic mixture of 96 mol% isobutane and 4 mol% propylene as the working fluid. This heat pump cycle comprises three brazed plate heat exchangers with a total heat transfer area of 134 m², two finned-tube heat exchangers, and a two-stage centrifugal compressor. The compressor features impellers with outer diameters of 61.9 mm for the first stage and 60.1 mm for the second stage.

Contents

Nomenclature

Symbols

Latin symbol	Definition	Unit
A	Area	m^2
B	Corrugation depth	m
Bd	Bond number	-
b	Blade height	m
b^*	Diffuser pinch	-
COP	Coefficient of performance	-
C	Absolute velocity	m s^{-1}
c_p	Specific heat capacity	kJ kg^{-1} K^{-1}
D	Diameter	m
D_h	Hydraulic diameter	m
F_T	LMTD correction factor	-
f	friction factor	-
G	Mass flux	kg m^{-2} s^{-1}
Gr	Grashof number	-
g	Gravitational acceleration	m s^{-2}
h	Specific enthalpy	kJ kg^{-1}
L	Lenght	m
L_{dry}	Energy loss dryer as % of total heat input	-
m	Mass	kg
$\dot{m}$	Mass flow rate	kg s^{-1}
N_s	Specific speed	-
Pr	Prandtl number	-
p	Pressure	Pa
$\dot{Q}$	Rate of heat transfer	W
q	Heat flux	W m^{-2}
Re	Reynolds number	-
s	Specific entropy	kJ kg^{-1} K^{-1}
T	Temperature	K
$\bar{T}$	Average temperature	K
t	Tip clearence height	m
U	Overall heat transfer coefficient	W m^{-2} K^{-1}
U	Pheripheral speed	m s^{-1}
$\dot{V}$	Volumetric flow rate	m^3 s^{-1}
W	Realative velocity	m s^{-1}
$\dot{W}$	Rate of work	W
x	vapour fraction	-
Z	Number of blades	-
Greek symbol	**Definition**	**Unit**
α	Heat transfer coefficient	W m^{-2} K^{-1}
β	Cheveron angle of plate	rad
Γ	Surface tension	N m^{-1}
γ	Heat capcaity ratio	-
Δ	Difference	-
δ	Thickness	m

η	Efficiency	-
ϑ	Temperature	°C
Λ	Wave lenght of plate corrugation	m
λ	Thermal conductivity	W m^{-1} K^{-1}
μ	Dynamic viscosity	kg m^{-1} s^{-1}
Π	Pressure ratio	-
ρ	Density	kg m^{-3}
$\dot{\sigma}$	Rate of entropy production	W K^{-1}
Φ	Area enlargement factor	-
φ	Relative humidity	-
χ	Peripheral absolute velocity to peripheral velocity ratio	-
ω	Angular velocity	rad s^{-1}
ω_{hum}	Absolute humidity	kg kg^{-1}

Subsripts

Subscript	Definition	Subscript	Definition
0	Reference point	hm	Heat exchanger material
1	Impeller inlet	hub	Blade hub
2	Impeller outlet	in	Inlet conditions
3	Diffuser outlet	is	Isentropic
a	Air	L	Liquid
acc	Acceleration	lm	Logarithmic mean
avg	Average	m	Mean
b	Blade	out	Outlet conditions
bl	Blade loading	p	Pinch
c	Cold stream	pl	Plate
comp	Compressor	r	Radial
cond	Condenser	rec	Recirculated
crit	Critical	sat	Saturated
db	Dry bulb	sf	Skin friction
df	Disk friction	SH	Super-heated
diff	Diffuser	sink	Quantity delivered by a system
dp	Dew point	source	Quantity taken by a system
evap	Evaporator	sp	Single-phase
exp	Expansion valve	st	Stage
f	Fouling	tc	Tip clearance
fric	Friction	tip	Blade tip
g	Gravitational	tp	Two-phase
gc	Gas cooler	u	Peripheral
gl	Glide	V	Vapour
h	Hot stream	w	Water
HEX	Heat exchanger	wf	Working fluid

Abbreviations

Abbreviation	Definition
EoS	Equation of state
GWP	Global warming potential
HC	Hydrocarbon
HEX	Heat exchanger
HTF	Heat transfer fluid
HTHP	High-temperature heat pump
IHX	Internal heat exchanger
LMTD	Logarithmic mean temperature difference
ODP	Ozone depletion potential
VCHP	Vapour compression heat pump

1

Introduction

The International Energy Agency estimated that the industry emitted nine gigatons (Gt) of CO_2 in 2022 (IEA, 2023). To limit global warming to a maximum of 1.5 °C, these emissions must be reduced by 45% by 2030, to achieve net-zero emissions by 2050 (United Nations, n.d.). The industry needs to begin electrifying its processes and utilising renewable energy sources to reach these targets.

The drying process is one of the most energy-intensive operations in various industries. In countries such as the United States, Canada, France, and the United Kingdom, energy consumption for drying typically represents 10-15% of the total energy used in the industry. This percentage can increase to 20-25% in countries like Denmark and Germany (Mujumdar, 2007). A substantial portion of this energy is derived from natural gas; in fact, 5% of the total natural gas consumption in the United States is utilised in indirect gas-fired dryers (Chudnovsky et al., 2020). The six industries that account for the largest share of energy consumption due to drying are detailed in Table 1.1.

Table 1.1: Share the total energy used for industrial drying and CO_2 emission per industry.

Industry	**Share of total energy used for industrial drying (%) (Bück, 2016)** [a]	**Total CO_2 emissions by sector (Mt)**
Pulp & Paper	33	150 (IEA, 2023)
Food & Agricultural	12	217 (IEA, 2023)
Wood processing	11	22 (IEA, 2023)
Ceramic	11	400 (IEA, 2007)
Chemical	6	1330 (IEA, 2023)
Textile	5	51 (IEA, 2023)

[a] The missing 22% in total energy used for industrial drying represents the energy consumed by all other drying industries.

The temperatures involved in industrial drying typically range from 60 °C to 200 °C, with about 60% of the total input energy being rejected as waste heat at temperatures below 100 °C (Wang et al., 2024). This temperature range, coupled with the high percentage of waste heat, makes heat pumps the preferred technology for electrifying the industrial drying process (Marina et al., 2021).

A heat pump typically delivers much more heat than the electricity it consumes, making it an exceptionally efficient solution for converting power to heat. However, the economic conditions for heat pumps are often unfavourable due to many countries' high electricity-to-gas cost ratio, along with relatively long payback periods (more than 3 years) (Jesper et al., 2021). Therefore, improving the efficiency of heat pumps is essential to bridge this gap.

Numerous studies have investigated and optimised high-temperature heat pumps for electrifying industrial processes. The research conducted by Vieren et al. (2023) focuses on the integration and optimisation of a high-temperature single-stage transcritical heat pump in three industrial processes

with large temperature glides: thermal oil heating, superheated steam drying and spray drying. Vieren et. al evaluated all fluids available in REFPROP 10.0. Ganesan et al. (2023) and Y. Huang et al. (2025) researched how using zeotropic mixtures in a high-temperature cascade heat pump could influence the performance without a specific industrial case. Ganesan et al. only evaluated two zeotropic mixtures in the upper and lower cycles of the cascade heat pump, whereas Y. Huang et al. evaluated six mixtures in the upper cycle and ten in the lower cycle.

In the research conducted by Hoang et al. (2025), a cascade heat pump was integrated and optimised for a spray dryer requiring a supply air temperature of 200 °C, which was heated from an ambient air temperature of 15 °C. The study aimed to identify the most suitable fluids for the upper and lower cycles of a cascade system by evaluating eleven pure fluids for the upper cycle and seven pure fluids for the lower cycle. Hoang et al. also assessed the total investment costs by calculating the installed costs for the compressors based on their volumetric flow rates. Additionally, the installed costs of heat exchangers were determined by their heat transfer area, using assumed heat transfer coefficients.

In a study conducted by Widdows (2024), a single-stage heat pump was integrated and optimised for a spray dryer that requires a supply air temperature of 180 °C, starting from an ambient temperature of 10 °C. Widdows' research is comparable to that of Hoang et al. (2025) in terms of dryer temperature and type; however, a key difference is Widdows' focus on optimising the heat pump cycle through the transcritical operation of zeotropic mixtures. Widdows evaluated 78 zeotropic mixtures and achieved a coefficient of performance (COP) of 3.38, while the best-performing cycle identified by Hoang et al. reached a COP of only 2.42. It's important to note that Hoang et al. used a heat transfer fluid in their heat pump cycle, which contributed to the lower COP. Nonetheless, the significant difference in performance suggests that integrating transcritical operation with zeotropic mixtures can enhance the performance of heat pumps.

Hoang et al. (2025) and Widdows (2024) investigated open heat pump dryers, which do not recycle the air that exits the dryer. Ni et al. (2025) conducted a study aimed at optimising a closed heat pump dryer, in which all humid air is recirculated, using zeotropic mixtures. However, their research was focused on achieving a supply air temperature of 70 °C. Logie et al. (2016) discusses a combination of the open and closed heat pump dryer in their paper on developing a test bench to demonstrate the potential for energy optimisation in heat pump dryers. They propose, among other configurations, a heat pump dryer that incorporates an evaporator bypass, allowing it to recirculate most of the humid air out of the dryer without cooling it.

Recent research has shown the potential of heat pumps to electrify industrial processes and integrate them effectively into drying cycles. However, significant gaps still exist in this area. This study will focus on the following objectives:

- A high-temperature heat pump will be integrated into a drying cycle that includes an evaporator bypass and recirculates most of the humid air exiting the dryer. Although Logie et al. (2016) discusses this type of heat pump dryer, no optimisation of the heat pump itself is addressed.
- Two types of heat pump cycles will be optimised: the single-stage heat pump and the cascade heat pump, utilising zeotropic mixtures and transcritical operation. The only study that incorporates zeotropic mixtures and transcritical operation is by Widdows (2024), which focuses solely on optimising a single-stage heat pump cycle. Additionally, this study will explore a drying cycle that differs significantly from Widdows' optimisation of an open heat pump dryer.
- This research does not assume isenthalpic drying, unlike all the studies mentioned.
- The heat exchangers and compressors will be appropriately sized. Only Hoang et al. (2025) performed sizing calculations for heat pump components, but those calculations relied on assumed heat transfer coefficients. In contrast, this study will conduct a more detailed analysis of the sizes of these components.

Focusing on these research gaps, this study aims to answer the following research question:

> *What is the optimal vapour compression heat pump cycle, considering configuration, working fluid selection, and component choice and sizing, for a non-isenthalpic industrial drying process?*

To answer this research question, the following four sub-questions are formulated:

1. How do modifications to the cycle, such as a multi-stage heat pump configuration and adding an internal heat exchanger, influence performance?
2. Does using zeotropic mixtures and transcritical operation of the heat pump improve performance?
3. What heat exchanger type should be used in the heat pump, and what is the sizing of the heat exchangers needed?
4. Which type of compressor is best suited for the required heat load and temperature range, and what should the design be regarding the number of stages and size?

Following this introduction, the thesis is organised into five additional chapters. Chapter 2 presents a theoretical framework that covers the drying cycle, various heat pump cycles and their components, and methods for evaluating and improving heat pump performance. Chapter 3 outlines the methodology for simulating two distinct heat pump cycles, optimising these cycles, and simulating the compressors and heat exchangers. Chapter 4 presents the results of the simulations and optimisation of both the single-stage and cascade heat pump cycles. This chapter includes a sensitivity study that illustrates the effects of dryer losses and the dew point temperature in the dryer. Chapter 5 concludes the research and discusses the findings. Finally, Chapter 6 offers recommendations for future research on this topic.

2

Theoretical framework

This chapter first explains how to integrate the heat pump into the dryer and obtain the required thermodynamic states of the humid air. Then, an overview of a basic heat pump cycle is provided, and the cascade heat pump cycle and internal heat exchanger are introduced. The following section explores the irreversibilities present in a heat pump cycle, discusses how performance can be measured, and examines methods to reduce entropy production in the heat exchangers. The chapter then evaluates potential working fluids for the heat pump cycle. The last section provides a detailed discussion of the three key components of the heat pump: the compressor, the heat exchangers and the expansion valve.

2.1. The drying cycle

To effectively integrate a heat pump into the dryer, it is essential to understand the thermodynamic properties of humid air at various stages of the drying process. Two key points to consider are the conditions before and after the dryer. Heat and mass transfer occur between the air and the drying product inside the dryer as water evaporates into the air. This evaporation increases the absolute humidity, which can be calculated as

$$\omega_{\text{hum}} = \frac{m_{\text{w}}}{m_{\text{a}}}. \tag{2.1}$$

Here, m_{w} is the mass of water vapour and m_{a} the mass of dry air. Another way to express the amount of water evaporated in the air is relative humidity φ, defined as the ratio of the partial water vapour pressure p_{w} to the saturated water vapour pressure $p_{\text{w,sat}}$ for a specific temperature. Key temperatures in the drying process include the dry bulb temperature ϑ_{db}, which is measured by a standard thermometer, and the dew point temperature ϑ_{dp}, indicating the temperature at which condensation occurs due to the air's inability to hold additional water vapour.

To identify the thermodynamic properties of humid air at various stages in the drying process, a company specialising in sustainable packaging solutions has provided relevant data and assumptions to define a realistic drying cycle. The data they provided is outlined in Table 2.1.

The dryer's dew point temperature of 85 °C indicates a drying process under high absolute humidity conditions. To maintain this humidity, much of the humid air exiting the dryer bypasses the evaporator and is directly recirculated through the condenser, as shown in the process flow diagram in Figure 2.1. Only a small portion of the air goes through the evaporator for heat recovery. Based on the mass and energy balances, the total thermal energy required from the heat pump is 530 kWth. The thermodynamic state at point 5 remains undetermined, as it relies on the energy recovered by the evaporator.

Table 2.1: Parameters used in simulating the drying cycle.

Pressure of the air	1 bar	p_{a}
Mass flow of humid air recirculated	5 kg/s	$\dot{m}_{\text{rec}}$
Mass flow of humid air through the evaporator	0.329 kg/s	$\dot{m}_{evap}$
Temperature of leaking into the drying cycle*	15 °C	$\vartheta_{\text{db},6}$
Relative humidity of air leaking into the drying cycle*	60%	φ_6
Mass flow of humid air leaking into the drying cycle*	0.180 kg/s	$\dot{m}_6$
Dew point temperature at point 3	85 °C	$\vartheta_{\text{dp},3}$
Temperature at point 3	120 °C	$\vartheta_{\text{db},3}$
Energy loss dryer as % of total heat input	20%	L_{dry}

* Value is based on an assumption, not on input from the industry.

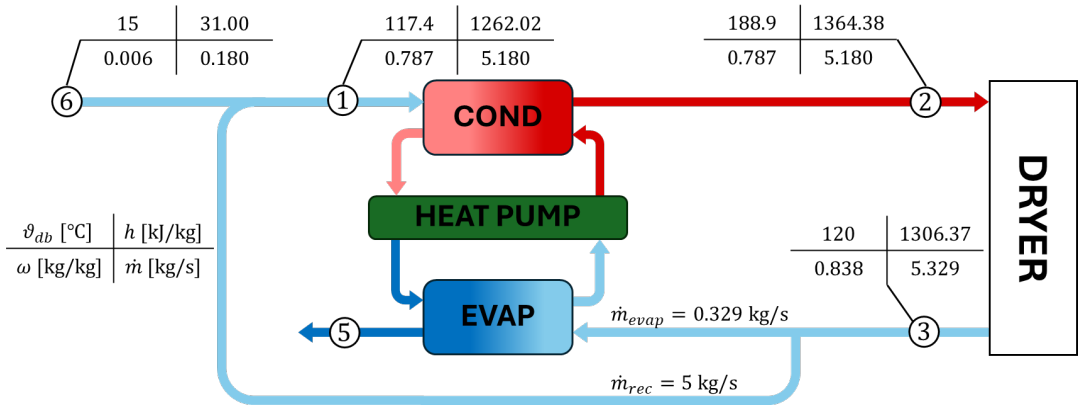

Figure 2.1: Process flow diagram of heat pump dryer with evaporator bypass and recirculation. All mass flows are in kilograms of humid air per second, and all enthalpies are in kilojoules per kilogram of humid air.

Figure 2.2 illustrates the Mollier diagram for the drying process. The green arrow indicates the non-isenthalpic drying as it deviates from the blue dotted isenthalpic line. The mass flow at point 6 is adjusted so that when mixed with the recirculated stream from point 3, the absolute humidity at point 1 returns to its original value. The blue arrow represents heat recovery in the evaporator, where first the humid air is cooled to its dew point. After that, most of the energy recovery occurs as water condenses from points 4 to 5, releasing latent heat. This results in a sharp temperature drop in the TQ diagram up to point 4, followed by a gradual slope from point 4 to point 5.

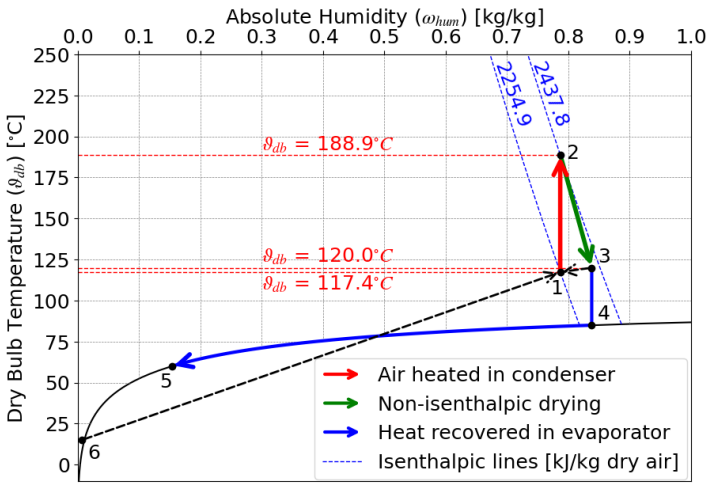

Figure 2.2: Mollier diagram of the heat pump dryer with evaporator bypass and recirculations. The dry bulb temperature at point 5 is assumed to be 60 °C. The actual temperature at Point 5 will depend on the heat needed to evaporate the working fluid. Isenthalpic lines are expressed in kJ/kg of dry air, unlike the enthalpies shown in Figure 2.1.

2.2. Heat pump cycles

Heat pumps work by elevating the temperature of a heat source, which can be a waste heat stream, using either heat or electricity. A common type of heat pump that uses electricity to increase heat is the vapour compression heat pump (VCHP), as illustrated in Figure 2.3. In this cycle, the waste heat is absorbed by the working fluid in the evaporator. Electricity is then used to increase the temperature and pressure of the working fluid through compression. The heated working fluid releases heat to the condenser's process stream, the heat sink. When the temperature of this process stream exceeds 100 °C, it is classified as a high-temperature heat pump (HTHP) (Zühlsdorf, 2023). Finally, the working fluid undergoes expansion, which lowers its pressure and temperature. The working fluid is expanded until its temperature falls below that of the heat source, allowing heat to be transferred from the heat source to the working fluid again, thereby completing the cycle.

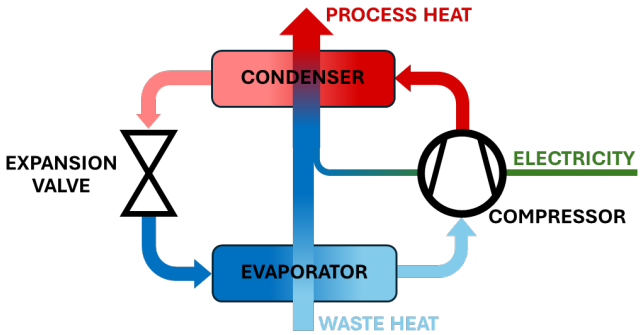

Figure 2.3: Schematic drawing of a single-stage vapour compression heat pump cycle.

In its simplest form, the VCHP cycle consists of four main components: the compressor, the condenser, the expansion valve, and the evaporator. This cycle is referred to as a single-stage heat pump. When there is a significant temperature difference between the heat source and sink, a cascade heat pump can improve performance compared to a single-stage heat pump, as shown by Ganesan et al. (2023) and Y. Huang et al. (2025). The cascade heat pump consists of two or more single-stage heat pump cycles working in tandem. In this arrangement, the condenser of one cycle acts as the evaporator for the next. Additionally, a cascade heat pump allows for different working fluids in each cycle.

Another method to enhance a heat pump's performance is to use an internal heat exchanger (IHX). A process flow diagram of a single-stage heat pump featuring an IHX is illustrated in Figure 2.4. This diagram shows the IHX transferring heat from the high-pressure liquid to the low-pressure gas. The purpose of the IHX is to lower the temperature of the working fluid before it enters the expansion valve, allowing the working fluid to end up further to the left in the two-phase region after expansion. Additionally, the IHX helps prevent wet compression by superheating the gas before it enters the compressor.

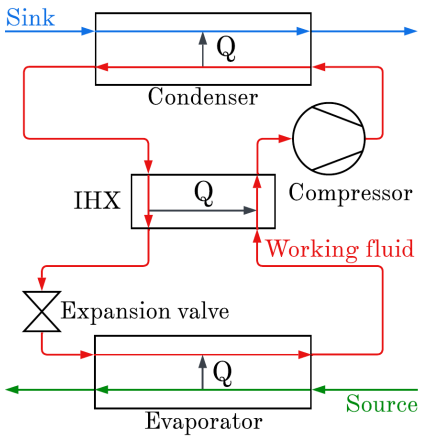

Figure 2.4: Process flow diagram of a single-stage heat pump with internal heat exchanger.

A heat transfer fluid (HTF) loop can be integrated into the heat pump cycle, allowing the heat pump to be located away from the dryer. This setup is particularly advantageous when dealing with highly flammable or toxic working fluids in the heat pump cycle. In the condenser, the HTF is heated by the working fluid and then transfers this heat to a heat sink through a heat exchanger (HEX) positioned away from the heat pump. A suitable HTF for the condenser is Therminol 66, which offers thermal stability at high temperatures and is resistant to fouling (Eastman, 2021). In the evaporator, the HTF transfers heat to the working fluid it receives from the source stream. Dowtherm Q is an appropriate choice for the evaporator loop, as its viscosity is lower at lower temperatures compared to Therminol 66 (Dow, 2020).

2.3. Peformance of the heat pump

This section introduces two methods for evaluating heat pump performance: the coefficient of performance and the second law of efficiency. It then discusses the losses in a heat pump cycle and explains how to calculate them. Finally, the section presents two approaches to reduce these losses in HEXs: using zeotropic mixtures and implementing transcritical heat pump cycles.

2.3.1. Performance evaluation

The performance of a heat pump is typically expressed as the coefficient of performance, commonly referred to as the COP. The COP is calculated as

$$COP = \frac{\dot{Q}_{\text{sink}}}{\dot{W}}, \tag{2.2}$$

where $\dot{Q}_{\text{sink}}$ represents the heat output and $\dot{W}$ denotes the work input. This formula serves as a reliable performance indicator for comparing different heat pump configurations operating at the same source and sink temperatures. When comparing heat pump cycles with varying source and sink temperatures, the second law efficiency can be used as a performance indicator, which is defined as

$$\eta_{\text{II}} = \frac{COP}{COP_{\text{Lorenz}}}. \tag{2.3}$$

The term COP_{Lorenz} refers to the theoretical maximum COP that can be achieved in a heat pump, assuming no irreversibilities are involved. According to the definition derived by Lorenz (1895), for heat pumps that operate with a temperature glide, the COP_{Lorenz} can be expressed as:

$$COP_{\text{Lorenz}} = \frac{\bar{T}_{\text{sink}}}{\bar{T}_{\text{sink}} - \bar{T}_{\text{source}}}. \tag{2.4}$$

In this context, $\bar{T}_{\text{sink}}$ and $\bar{T}_{\text{source}}$ refer to the average temperatures of the heat sink and heat source, respectively. As discussed in section 2.1, the temperature profile of the humid air passing through the evaporator is non-linear. Therefore, to determine the average temperature, the entropic average temperature formula needs to be used (Alefeld, 1987), defined as

$$\bar{T} = \frac{h_{\text{out}} - h_{\text{in}}}{s_{\text{out}} - s_{\text{in}}}. \tag{2.5}$$

2.3.2. Losses in heat pumps

There are losses in all the components of a heat pump. These losses can be quantified by calculating the entropy production, denoted as σ. In the compressor, entropy production arises from internal flow losses, heat transfer, conduction, mechanical friction, and internal leakage (Kiss & Infante Ferreira, 2016). These losses are often represented by the isentropic efficiency, which is calculated as

$$\eta_{\text{is}} = \frac{h_{\text{out,s}} - h_{\text{in}}}{h_{\text{out}} - h_{\text{in}}}. \tag{2.6}$$

In this equation, $h_{\text{out,s}}$ represents the enthalpy of the fluid exiting the compressor under ideal conditions, known as isentropic compression, where no losses occur. h_{in} is the enthalpy of the fluid entering the compressor. h_{out} indicates the actual enthalpy of the gas leaving the compressor. The total entropy production in the compressor is calculated as

$$\dot{\sigma}_{\text{comp}} = \dot{m}_{\text{wf}}(s_{\text{comp,out}} - s_{\text{comp,in}}), \tag{2.7}$$

where $s_{\text{comp,out}}$ and $s_{\text{comp,in}}$ refer to the specific entropy at the outlet and inlet of the compressor, respectively, and $\dot{m}_{\text{wf}}$ is the mass flow rate of the working fluid.

The entropy generated in the expansion valve arises from the expansion of the working fluid, during which no pressure energy is converted into mechanical work. Consequently, all pressure energy is lost in this process. The entropy produced in the expansion valve can be calculated as

$$\dot{\sigma}_{\text{exp}} = \dot{m}_{\text{wf}}(s_{\text{exp,out}} - s_{\text{exp,in}}), \tag{2.8}$$

where $s_{\text{exp,out}}$ and $s_{\text{exp,in}}$ represent the entropy at the outlet and inlet of the expansion valve, respectively.

Entropy production in a HEX, assuming no pressure loss and no energy loss to the surroundings, arises from the temperature difference between the hot and cold streams. The entropy production can be calculated using the following equation:

$$\dot{\sigma}_{\text{HEX}} = (s_{\text{h,out}} - s_{\text{h,in}})\dot{m}_{\text{h}} + (s_{\text{c,out}} - s_{\text{c,in}})\dot{m}_{\text{c}}. \tag{2.9}$$

In this equation, $s_{\text{h,out}}$ and $s_{\text{h,in}}$ represent the entropies at the outlet and inlet of the HEX for the hot stream, while $s_{\text{c,out}}$ and $s_{\text{c,in}}$ represent the entropies at the inlet and outlet for the cold stream.

The total entropy production of the heat pump, denoted as $\dot{\sigma}_{\text{total}}$, is the cumulative sum of the entropy production from all individual heat pump components. To verify the calculation of the total entropy production, the COP can be calculated using the method proposed by Alefeld (1987):

$$COP = \left(\frac{\bar{T}_{\text{sink}}}{\bar{T}_{\text{sink}} - \bar{T}_{\text{source}}}\right)\left(1 + \frac{\bar{T}_{\text{source}}\bar{T}_{\text{sink}}}{\bar{T}_{\text{sink}} - \bar{T}_{\text{source}}}\frac{\dot{\sigma}_{\text{total}}}{\dot{Q}_{\text{sink}}}\right)^{-1}. \tag{2.10}$$

The numerical value obtained from this calculation should be compared to the COP calculated using Equation (2.2). If the entropy production within the heat pump is calculated correctly, both values should be equal.

2.3.3. Improving heat pump performance

Reducing total entropy production can enhance the efficiency of a heat pump. A significant amount of entropy is generated during heat transfer between the working fluid and the process stream, as well as between the waste stream and the working fluid (Zühlsdorf et al., 2018). As mentioned in section 2.3.2, this entropy production arises from the temperature difference between the hot and cold fluids. Therefore, minimising the temperature difference between these fluids leads to lower entropy production.

When a gradient exists in the fluid's temperature profile, the process of reducing the temperature difference between the hot and cold fluids is known as glide matching. Figure 2.5 illustrates the difference between heat transfer with and without glide matching. A comparison of the temperature profiles shown in Figures 2.5a and 2.5b demonstrates that the temperature of the glide-matched working fluid more closely aligns with the heat sink temperature profile.

One effective method for achieving glide matching is the use of zeotropic mixtures. These mixtures consist of fluids with differing boiling points, which creates a temperature glide within the two-phase region, as illustrated in Figure 2.6a. The slope of this glide can be modified by adjusting the composition of the mixture. Numerous studies have investigated the use of zeotropic mixtures for glide matching.

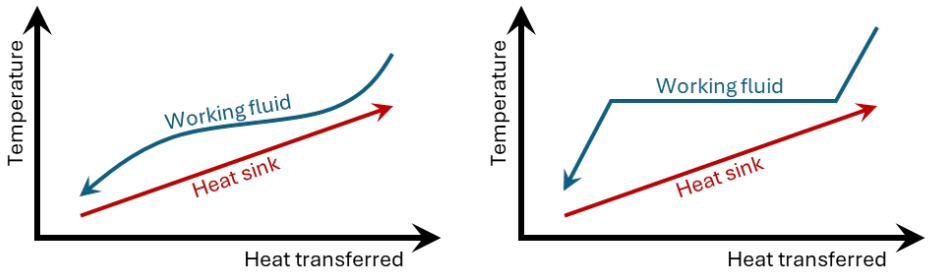

(a) TQ diagram of heat transfer with glide matching.

(b) TQ diagram of heat transfer without glide matching.

Figure 2.5: Illustration of the difference between heat transfer with and without glide matching.

Zühlsdorf et al. (2018) reported performance improvements of up to 27% in a single-stage heat pump when employing zeotropic mixtures for glide matching.

Additionally, Y. Huang et al. (2025) examined zeotropic mixtures in a cascade heat pump to enhance heat production up to 200 °C. Their research indicated that this method resulted in a 9.55% increase in the COP compared to a standard cascade heat pump system without glide matching. Glide matching with zeotropic mixtures is especially advantageous for applications where the temperature profile isn't too steep, as the glide is constrained by the difference in boiling points of the mixture's components.

As the temperature profile becomes steeper, operating the working fluid above its critical temperature, known as a transcritical cycle, is more effective. In this context, "transcritical" refers to a cycle that transfers heat to a sink while the working fluid is in a supercritical state and absorbs heat when it is in a subcritical state. Figure 2.6b illustrates an example of this cycle. In a transcritical cycle, the condenser is referred to as a gas cooler, as no phase change occurs during this process. Instead, the properties of the fluid change significantly when it crosses the Widom line, a virtual line where abrupt changes in characteristics take place (Banuti, 2015). Zhao et al. (2024) demonstrated these significant changes in density, specific heat capacity, thermal conductivity, and viscosity and discussed how to factor these changes into the design of a gas cooler.

If glide matching is desired in both the condenser and the evaporator, both methods can be used simultaneously by employing a zeotropic mixture in a transcritical cycle. Research conducted by Widdows (2024) demonstrated that combining these methods improved performance by up to 21.47%. In his study, Widdows simulated heat pump cycles in which the working fluid's temperature decrease in the gas cooler ranged from 100 °C to 160 °C, and the temperature increase in the evaporator ranged from 25 °C to 55 °C.

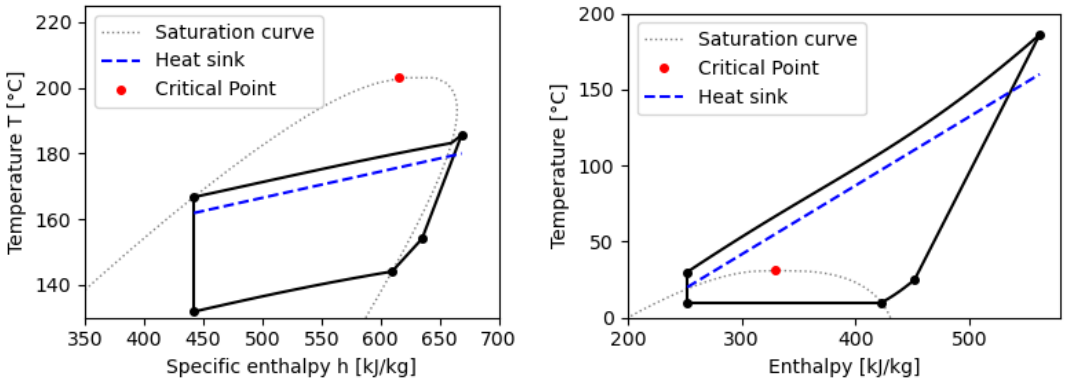

(a) T-h diagram of a heat pump cycle showing glide matching by using a zeotropic mixture of butane and hexane.

(b) T-h diagram of a heat pump cycle showing glide matching by transcritical operation of CO_2.

Figure 2.6: T-h diagrams illustrating the effect of using a zeotropic mixture and a transcritical cycle on glide matching.

2.4. Working fluid selection

Section 2.3.3 addresses using zeotropic mixtures and transcritical cycles to improve heat pump performance. Implementing these methods requires selecting the appropriate fluid or fluid mixture that matches the heat pump's thermal duty. In addition to thermodynamic properties, environmental considerations should be taken into account when selecting the working fluid.

Traditionally, hydrochlorofluorocarbons (HCFCs) and Chlorofluorocarbons (CFCs) were used as working fluids in heat pumps and refrigeration cycles (Kubba, 2017). Under the "Montreal Protocol on Substances that Deplete the Ozone Layer Final Act 1987" (1989), these fluids were phased out because of their ozone depletion potential (ODP). Alternatives were found in hydrofluorocarbons (HFCs), possessing a low ODP. However, this group of working fluids has a high Global Warming Potential (GWP), resulting in their inclusion in the Montreal Protocol in 2016 under the Kigali Amendment. New alternatives are found in hydrofluoroolefins (HFOs) and hydrofluoroethers (HFEs) as they have zero ODP and low GWP. A potential problem, however, with these working fluids is that they contain carbon-fluorine bonds, making them part of the Per- and polyfluoroalkyl substances (PFAS). The carbon-fluorine bonds are one of the strongest in organic chemistry, making them resistant to degradation, which can lead to potential health and environmental risks. These risks are the reason for the intention to restrict the use of PFAS in the European Union (ECHA, 2023). The (potential) restrictions on the fluids mentioned above leave only natural refrigerants as an option. Commonly used natural refrigerants are listed in Table 2.2, of which most are hydrocarbons (HCs).

To optimise the heat pump cycles, mixtures of the natural refrigerants listed in Table 2.2 will be utilised. Combining all 13 fluids in pairs results in 78 unique zeotropic mixtures. Section 3.2 will explain how these zeotropic mixtures will be applied in the optimisation process.

Table 2.2: This is a list of natural refrigerants organised by reference number. Natural refrigerants classified as hydrocarbons are indicated with "HC" under the "Type" column. The GWP_{100} (Global Warming Potential over a 100-year period, compared to CO_2) is included, along with safety class information, which is adapted from Zühlsdorf et al. (2018). Additionally, the critical temperature and pressure values are sourced from REFPROP 10.0 (Lemmon, Bell, et al., 2018).

Name of Fluid	Ref. No.	Type	GWP_{100yr}	Crit. Temp. (°C)	Crit. Press. (bar)	Safety Class	EoS used by REFPROP
Methane	R-50	HC	25	-82.6	46.0	A3	Setzmann and Wagner (1991)
Ethane	R-170	HC	2.9	32.2	48.7	A3	Bücker and Wagner (2006)
Dimethyl ether	R-E170	HC	1.0	127.2	53.4	A3	Wu et al. (2011)
Propane	R-290	HC	3.0	96.7	42.5	A3	Lemmon et al. (2009)
Butane	R-600	HC	4.0	152.0	38.0	A3	Bücker and Wagner (2006)
Iso-Butane	R-600a	HC	3.0	134.7	36.3	A3	Bücker and Wagner (2006)
Pentane	R-601	HC	4.0	196.6	33.7	A3	Thol et al. (2018a)
Iso-Pentane	R-601a	HC	4.0	187.2	33.8	A3	Lemmon and Span (2006)
Hexane	R-602	HC	4.0	234.7	30.4	A3	Thol et al. (2018b)
Ammonia	R-717	–	0	132.4	113.6	B2L	Gao et al. (2020)
CO_2	R-744	–	1.0	31.0	73.8	A1	Span and Wagner (1996)
Ethylene	R-1150	HC	6.8	9.2	50.4	A3	Smukala et al. (2000)
Propylene	R-1270	HC	3.1	91.1	45.6	A3	Lemmon, Mclinden, et al. (2018)

2.5. Components of the heat pump

This section covers three essential components of a heat pump: the HEX, the compressor and the expansion valve. First, the heat exchanger will be discussed, and a method for calculating its size will be explained. Then, different compressors are evaluated, focusing on their working principles and operating ranges. The last part evaluates two different expansion valves.

2.5.1. Heat exchangers

A HEX plays a crucial role in a heat pump by facilitating the transfer of energy between fluids. The total energy transferred can be expressed as

$$\dot{Q} = \dot{m}_{\mathrm{h}} \Delta h_{\mathrm{h}} = \dot{m}_{\mathrm{c}} \Delta h_{\mathrm{c}}, \tag{2.11}$$

where $\dot{m}$ represents the mass flow rate and Δh denotes the specific enthalpy difference between the fluid entering and exiting the HEX. The efficiency of heat transfer from the hot fluid to the cold fluid is determined by the overall heat transfer coefficient U. The overall heat transfer coefficient can be visualised as a series of thermal resistances, where each resistance contributes to a temperature difference, as illustrated in Figure 2.7.

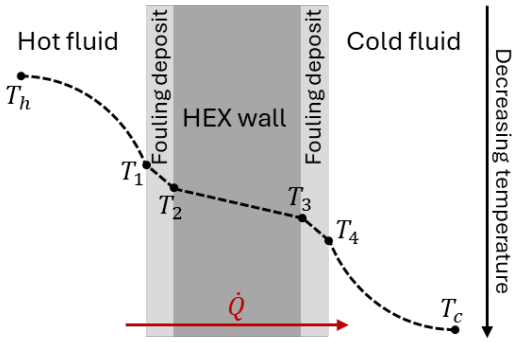

Figure 2.7: Temperature profile in a HEX with fouling on both sides of the wall.

The convective heat transfer coefficients govern the thermal resistances of the hot and cold fluids. The thermal resistance of the fouling layer and the HEX wall is determined by their thermal conductivities and the thickness of the respective layers. Using the principles of thermal resistance, the overall heat transfer coefficient can be calculated as

$$U = \frac{1}{\frac{1}{\alpha_\mathrm{h}} + \frac{\delta_\mathrm{hm}}{\lambda_\mathrm{hm}} + \frac{1}{\alpha_\mathrm{c}} + \sum \frac{\delta_\mathrm{f}}{\lambda_\mathrm{f}}}. \tag{2.12}$$

In this equation, α_h and α_c represent the heat transfer coefficients for the hot and cold fluids, respectively. The term δ_hm denotes the thickness of the HEX wall that separates the two fluids, while λ_hm refers to the thermal conductivity of the HEX material. Additionally, δ_f and λ_f indicate the thickness and thermal conductivity of the fouling layers. The contributions of all fouling types are summed in Equation (2.12) to determine the total thermal resistance.

Various types of fouling can occur in a HEX, depending on the fluid and the material used for the HEX. The most common types, as described by Ogunedo (2020), include:

- Scaling results from crystallising salts dissolved in the fluid. Temperature variations can affect the fluid's solubility, consequently causing salt crystals to be deposited on the surface of the HEX.
- Particulate fouling occurs when solid particles, such as dust, dirt, or rust, deposit on the surface of the HEX. The source of the fluid significantly influences the size of these particles; for instance, water from a river contains much larger particles than those found in an oil stream.
- Corrosion fouling arises from the considerable growth of a layer of corrosion products on the surface. An example of this is the oxide coating that protects the metal. As the thickness of this protective layer increases excessively, fouling issues emerge.
- Chemical fouling occurs when chemical reaction rates rise due to a higher temperature near the wall than in the bulk and a lower flow velocity in the boundary layer, resulting in foul deposition.
- Freezing fouling happens when a fluid stream is cooled below its solidification temperature and thus starts to freeze onto the HEX surface.
- Biofouling refers to the growth of organisms, including algae and fungi, on the surface of HEXs. These deposits create a favourable environment for bacterial activity and typically occur in humid conditions.

The heat transfer coefficients, α_h and α_c, are influenced by the thermal properties of the fluids, the geometry of the HEX, and the flow rate. Correlations can be found in the literature to determine the heat transfer coefficient. These correlations are often developed for specific types of HEX and flow regimes.

When the temperatures of the incoming and outgoing hot and cold streams in the HEX are completely specified, utilising the heat transferred $\dot{Q}$ and the overall heat transfer coefficient U, the total required heat transfer area can be determined by

$$\dot{Q} = UA\Delta T_{\mathsf{m}}, \tag{2.13}$$

where A denotes the heat transfer area and ΔT_{m} the mean temperature difference. The mean temperature difference for a pure counter-flow HEX is computed using the LMTD method as

$$\Delta T_{\mathsf{m}} = \Delta T_{\mathsf{lm}} = \frac{(T_{\mathsf{h,out}} - T_{\mathsf{c,in}}) - (T_{\mathsf{h,in}} - T_{\mathsf{c,out}})}{\ln \frac{T_{\mathsf{h,out}} - T_{\mathsf{c,in}}}{T_{\mathsf{h,in}} - T_{\mathsf{c,out}}}}, \tag{2.14}$$

where $T_{\mathsf{h,\,in}}$ and $T_{\mathsf{h,\,out}}$ represent the temperatures of the hot stream in and out of the HEX. Similarly, $T_{\mathsf{c,\,in}}$ and $T_{\mathsf{c,\,out}}$ denote the temperatures of the cold stream at the inlet and outlet of the HEX. When the flow configuration is not strictly counter-current, the logarithmic mean temperature difference (LMTD) must be adjusted using a correction factor F_T (Bowman et al., 1940; Underwood, 1934), as

$$\Delta T_{\mathsf{m}} = F_T \Delta T_{\mathsf{lm}}. \tag{2.15}$$

This correction factor depends on the flow geometry and whether the system operates under multi-phase or single-phase flow conditions. Typically, F_T is represented in charts. Among others, Hewitt et al. (1994) and Taborek (1994) have published books regarding this correction factor for various HEX configurations.

HEX selection for the heat pump cycle

The working fluid in the heat pump's closed loop will consist of zeotropic mixtures of natural refrigerants, as outlined in section 2.4. On the other side of the evaporator and condenser/gas cooler, the heat transfer fluids (HTFs) will be either Therminol 66 or Dowtherm Q, as discussed in section 2.2. Neither the working fluid nor the HTFs will contain large particles that could lead to fouling. When ammonia is used as the working fluid, no copper alloys should be used because of the risk of corrosion fouling (Stoecker, 1998). Additionally, the combination of ammonia and carbon dioxide should be avoided, as it can result in chemical fouling (Brooks et al., 1946). Since the working fluid and HTF will be free of salts and organisms, issues such as scaling and biofouling will not arise. Furthermore, freezing fouling is not a concern, as these fluids will not solidify at the operational temperatures.

The risk of fouling in the heat pump's condenser, evaporator and IHX is very low. The low risk of fouling enables the use of plate HEXs, which are renowned for their high thermal efficiency and compact design. For applications requiring pressures of up to 25 bar, a gasketed plate HEX is suitable (Arsenyeva et al., 2023). This type consists of plates pressed together with a gasket in between, creating sealed channels. An illustration of the gasketed plate HEX is given in Figure 2.8a.

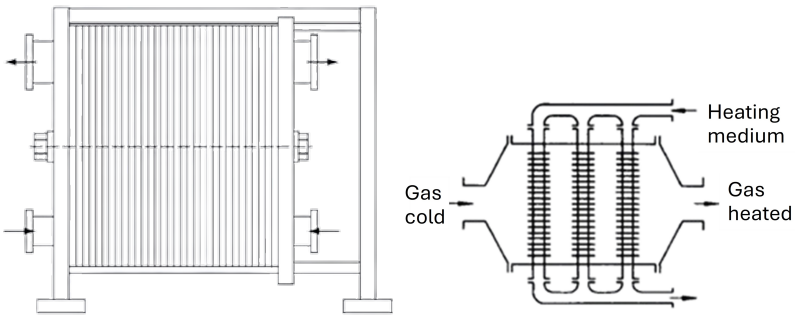

(a) Plate HEX (Roetzel & Spang, 2010). **(b)** Finned tube HEX (Roetzel & Spang, 2010).

Figure 2.8: Illustrations of different HEX types.

Brazed or semi-welded plate HEXs are an alternative to gasketed plate HEXs and can be used when higher pressures are necessary. Brazed plate HEX can support pressures up to 90 bar, while semi-welded plate HEX can handle pressures up to 63 bar (Arsenyeva et al., 2023). In a brazed HEX, the plates are bonded together through a brazing process, ensuring a seal around the plate edges. In a semi-welded plate HEX, two plates are bonded together by welding to create a channel for the high-pressure fluid. The low-pressure channels in a semi-welded plate HEX are formed by pressing two sets of welded plates with a gasket in between, similar to the gasketed plate HEX.

To heat the humid air and recover heat from the air stream exiting the dryer, two HEXs are required. Since the air used in the dryer is drawn in from the surrounding environment, there is a high likelihood of particulate fouling. The combination of warm, moist air and the potential for biological organisms creates a significant risk of biofouling. Additionally, corrosion fouling can occur when materials with an oxide coating are used for the HEX. However, the other three types of fouling are unlikely to happen on the air side.

Given the high risk of fouling and the low heat transfer coefficient of air, a finned tube HEX is necessary. An illustration of the finned tube HEX is shown in Figure 2.8b. This type of HEX is designed to handle fouling conditions, and the fins increase the heat transfer area, compensating for the air's low heat transfer coefficient.

2.5.2. Compressors

Compressors can be categorised into two main types: positive displacement compressors and dynamic compressors. Positive displacement compressors reduce the volume of a closed space, increasing pressure. In contrast, dynamic compressors transfer kinetic energy to the gas through rotating impellers or blades, which is then converted into increased pressure. Typical operating ranges for different compressors are given in Figure 2.9. In HTHP, the most commonly used types are the reciprocating and rotary screw compressors (El Samad et al., 2024). The rotary screw compressor covers the higher heating capacity range, as it can manage higher flow rates. A centrifugal compressor is used to achieve even greater heating capacities.

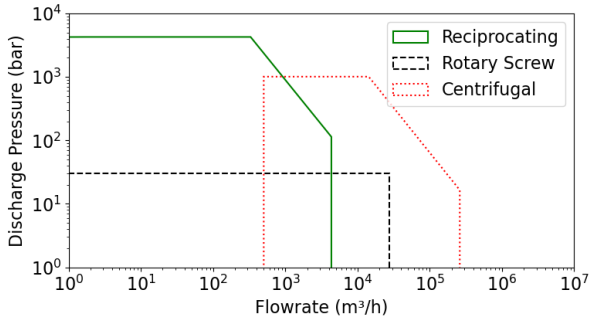

Figure 2.9: Typical coverage ranges for compressor types commonly used in HTHP. Actual ranges can differ from those given in the graph. Adapted from *GPSA engineering data book* (14th). (2017). Gas Processors Association.

When designing a compressor, the pressure ratio, defined as

$$\Pi = \frac{p_{\text{out}}}{p_{\text{in}}}, \tag{2.16}$$

is limited by the maximum temperature increase that occurs during each stage of the compression process. This limitation is crucial because the components must withstand the temperature differences generated during the compression process. The relationship between pressure and temperature during isentropic compression for an ideal gas is expressed as

$$\Pi^{\frac{\gamma-1}{\gamma}} = \frac{T_{\text{out}}}{T_{\text{in}}}, \tag{2.17}$$

where γ represents the heat capacity ratio, calculated as $c_\mathrm{p}/c_\mathrm{v}$. This relationship illustrates that the temperature increases more rapidly for gases with a higher heat capacity ratio. Multiple stages can be employed if the desired pressure ratio is too high to achieve in a single stage. The pressure ratio per stage for n stages is calculated as

$$\Pi_\mathrm{st} = \left(\frac{p_\mathrm{out}}{p_\mathrm{in}} \right)^{1/n}. \tag{2.18}$$

The reciprocating compressor is commonly used in HTHP due to its simplicity, efficiency, and low cost (Giampaolo, 2023). As shown in Figure 2.10a, it features a cylinder and a piston moved by a crankshaft. The compression process starts with opening the suction valve and increasing the volume by moving the piston, which allows the fluid to flow into the cylinder. Once the fluid has entered, the suction valve closes, and the piston moves upward to compress the fluid. Finally, the discharge valve is opened to release the pressurised fluid, and the cycle starts over. Because gas is not delivered continuously, the pulsations in flow and pressure can result in vibrations (Smith, 2016).

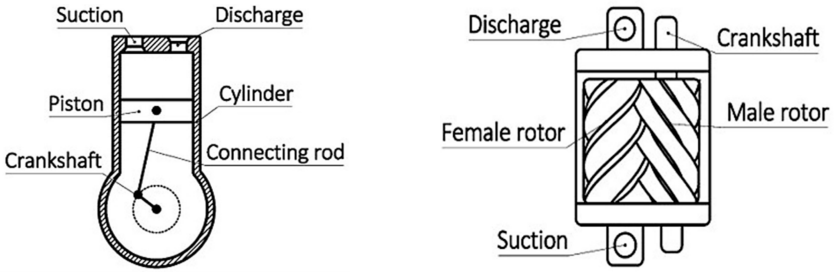

(a) Reciprocating compressor. **(b)** Rotary screw compressor.

Figure 2.10: Schematic drawings of two types of positive displacement compressors (Lu et al., 2023).

Reciprocating compressors, as illustrated in Figure 2.9, typically operate at the lower end of the volumetric flow range; however, when equipped with a crosshead, they can achieve discharge pressures of up to 3,400 bar (Hollingsworth et al., 2019). The heat capacity ratio influences the maximum pressure ratio, as described in Equation (2.17). For example, gases such as air, which has a γ of 1.4, can achieve a maximum compression ratio of 4 per stage, while butane, with a γ of 1.1, can reach compression ratios of up to 9. Furthermore, the maximum recommended discharge temperature for a reciprocating compressor is 175 °C (API, 2024). The isentropic efficiency, as defined in Equation (2.6), usually ranges from 70% to 90% (Peters et al., 2003), with efficiencies exceeding 90% observed in large industrial slow-speed reciprocating compressors. The primary sources of losses in these compressors are valve losses, which tend to decrease at higher pressure ratios and with lighter molecular weights (Hollingsworth et al., 2019).

The rotary screw compressor, illustrated in Figure 2.10b, is a positive displacement compressor commonly used for power levels from 10 to 500 kW and discharge pressures below 30 bar (Hollingsworth et al., 2019). It consists of two intermeshing helical lobes within a casing, which create compression chambers that reduce in volume as the rotors turn (Broerman et al., 2019). There are two types: oil-flooded and dry screw compressors. Oil-flooded compressors inject lubricating oil to create a film between the rotors, which is discharged with the pressurised gas, necessitating a separation process. In contrast, dry screw compressors operate without oil, requiring tighter rotor clearances and resulting in higher manufacturing costs. The isentropic efficiency of rotary screw compressors ranges from 65% to 75% (Campbell, 2014). Dry screw compressors can achieve discharge pressures exceeding 50 bar (Wennemar, 2009), with maximum compression ratios capped at 6 for HTHP applications (Sharevska et al., 2025). Oil-flooded compressors can reach compression ratios as high as 20, benefiting from the cooling properties of the lubrication oil. However, they must maintain a maximum discharge temperature of 180 °C to prevent oil degradation (Tijani et al., 2025).

The centrifugal compressor is a dynamic compressor commonly used in heat pumps with heating capacities that reach the megawatt range (Hollingsworth et al., 2019). The compression process begins

in the compressor's impeller, where the gas is accelerated and its kinetic energy is increased. This kinetic energy is converted into pressure energy as the gas decelerates in the diffuser. An illustration of the components can be found in Figure 2.11. Additionally, multiple stages of centrifugal compressors can be arranged along a common axis to achieve higher pressure ratios. Uusitalo et al. (2024) conducted simulations of centrifugal compressors utilised in transcritical CO_2 heat pumps with heating capacities ranging from 1 to 20 MW. Their findings predicted isentropic efficiencies ranging from 80% to over 85%. Notably, the lower isentropic efficiencies were observed in compressors designed for heat pumps with heating capacities below 3 MW. This reduction in efficiency is attributed to the smaller impellers used in these compressors, which lead to significant tip clearance losses.

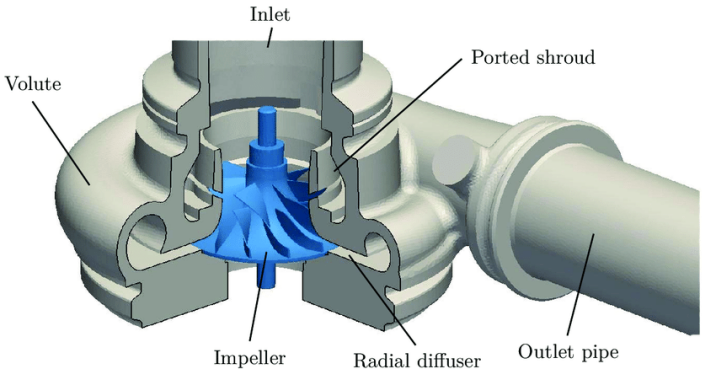

Figure 2.11: Illustration of a centrifugal compressor (Heinrich, 2016).

When selecting a compressor, the output temperature that must be reached is a crucial criterion. In section 2.1, it is established that the air temperature exiting the condenser must reach 188.9 °C. Accounting for the pinch temperatures, the working fluid must be compressed until a minimum temperature of 203.9 °C is reached. This minimum temperature rules out the use of reciprocating and screw compressors due to their maximum output temperatures of 175 °C and 180 °C, respectively, as outlined above. Consequently, the centrifugal compressor emerges as the only viable option for this heat pump design.

2.5.3. Expansion valve

The expansion valve regulates the flow and pressure difference between the high-pressure condenser and the low-pressure evaporator. In direct expansion circuits, the most commonly used types of expansion devices are thermostatic expansion valves and electronic expansion valves (Hundy et al., 2016).

The thermostatic expansion valve manages the flow of refrigerant by measuring the temperature of the working fluid as it exits the evaporator. This measurement occurs using a bulb that contains either the working fluid or a reference fluid with similar properties. As the temperature of the fluid leaving the evaporator varies, this affects the temperature and corresponding pressure inside the bulb. Since the bulb is connected to the valve via a capillary tube, changes in pressure cause a diaphragm within the valve to move. This movement adjusts the valve opening to maintain the desired level of superheating.

The electronic expansion valve, on the other hand, measures both the pressure and temperature at the evaporator outlet. Based on these measurements, an actuator adjusts the valve opening to achieve the desired pressure and temperature. The electronic valve can be programmed to optimise the system's performance across a broader capacity range, which results in a more efficient cycle compared to the thermostatic expansion valve. Although the electronic valve is generally more expensive, its increased efficiency results in lower energy costs, as demonstrated by Lazzarin and Noro (2008).

It is recommended to use the electronic expansion valve if the heat pumps proposed in this study are further developed, as this valve improves performance over a wide range of conditions. As the expansion valve will not be discussed further in this study, this section contains all the information about this component. In the heat pump simulation, isenthalpic expansion will be assumed to model the operation of the expansion valve.

3

Methodology

This chapter introduces the two heat pump cycles that will be optimised. It then examines the degrees of freedom to determine the temperatures that must be identified in the simulation. The following section discusses the optimisation of the heat pump cycles, detailing the optimisation parameters, the logic behind the optimisation, and an analysis of the mixture space. Finally, the chapter explains the methods for sizing compressors and heat exchangers.

3.1. Heat pump cycle simulation

Two heat pump cycles have been simulated and optimised: a single-stage and a cascade heat pump. Both systems feature an internal heat exchanger (IHX) that reduces the temperature of the high-pressure liquid, shifting the expansion valve's exit point to the left in the two-phase region. They also include a heat transfer fluid (HTF) loop, enabling the heat pump to be placed flexibly. As explained in section 2.2, Therminol 66 is used as the HTF in the condenser, while Dowtherm Q is used in the evaporator. The process flow diagrams for both cycles are shown in Figure 3.1.

In the simulation of the two heat pump cycles, the following assumptions have been made:

- The HEXs experience no pressure losses or heat losses to the surroundings.
- A pinch temperature is established in the HEXs, which varies based on whether they transfer heat with air. The pinch temperature when air is involved ($\Delta T_{\text{p,a}}$) is set at 10 °C due to air's relatively low heat transfer coefficient. HEXs that do not involve air have a pinch temperature ΔT_{p} of 5 °C.
- For the simulation of the expansion valve, isenthalpic expansion is assumed.
- The compressors have an isentropic efficiency of 80%.

3.1.1. Degrees of freedom analysis single stage cycle

The thermodynamics of the cycles have been analysed to define the degrees of freedom in the heat pump simulation. A summary of this thermodynamic analysis for the single-stage heat pump is presented in Table 3.1. From this analysis, it is evident that three key temperatures must be established: the temperature of the working fluid leaving the evaporator, T_1; the superheating temperature, ΔT_{SH}; and the temperature of the working fluid exiting the compressor, T_3. The temperatures T_1 and T_3 are adjusted iteratively to achieve the desired pinch point, while ΔT_{SH} is incrementally increased until the pinch point in the IHX is reached. The impact of these temperature adjustments is illustrated in the Ts diagram in Figure 3.2, which compares two heat pump cycles with different pinch points. The exact workings of the simulation code for the single-stage heat pump can be found in the flowchart presented in Figure A.1 of Appendix A.

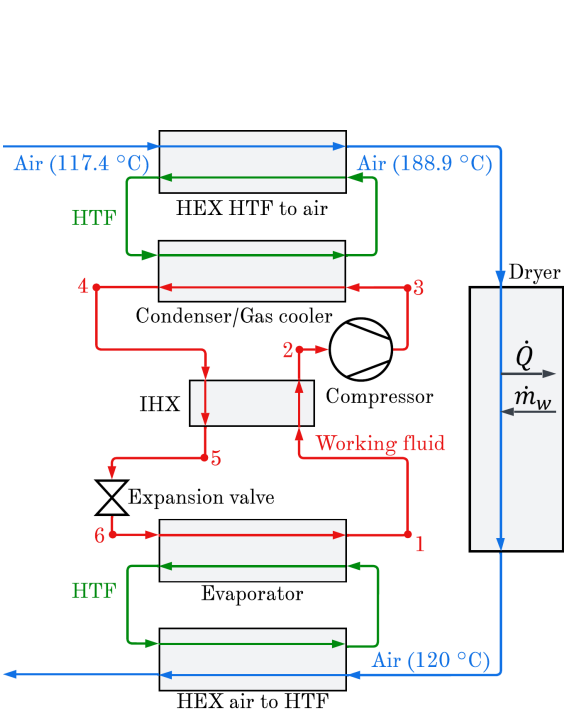

(a) Single-stage heat pump cycle with IHX and HTF.

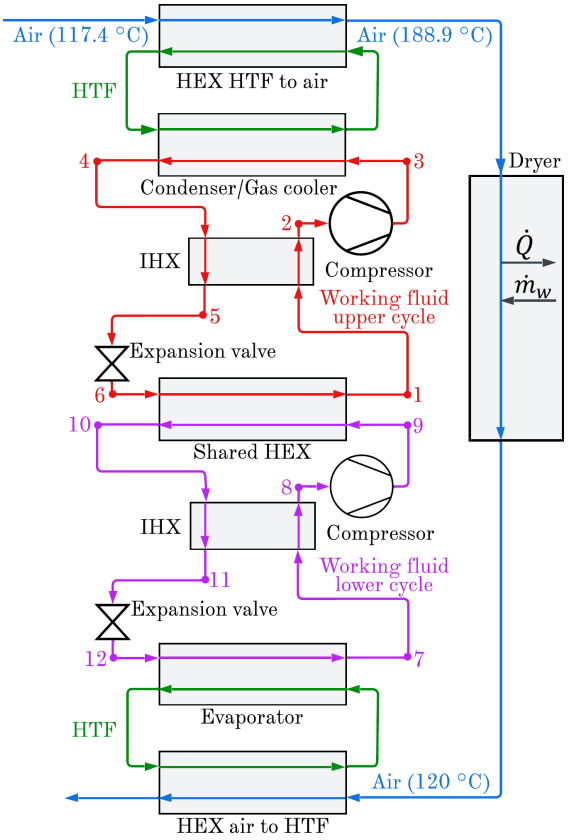

(b) Cascade heat pump cycle with IHX and HTF.

Figure 3.1: Proposed heat pump cycles with internal heat exchanger (IHX) and heat transfer fluid (HTF).

Table 3.1: Summary of the single-stage heat pump thermodynamic analysis.

Node / Component	Inputs	Solved	Calculated with REFPROP
1 (Evaporator outlet)	T_1, $x_1 = 1$	—	h_1, s_1, p_1
2 (Compressor inlet)	T_1, ΔT_{SH}, p_1	$T_2 = T_1 + \Delta T_{\text{SH}}$, $p_2 = p_1$	h_2, s_2
3 (Compressor outlet)	η_{is}, h_2, s_2, T_3	p_3 via iteration on $\eta_{\text{is}} = \dfrac{h_{3s} - h_2}{h_3 - h_2}$	$h_{3s} = h(p_3, s_2)$, h_3, s_3
4 (Condenser outlet)	$T_{\text{air,in}}$, $\Delta T_{\text{p,a}}$, ΔT_{p}, p_3	$T_4 = T_{\text{air,in}} + \Delta T_{\text{p,a}} + \Delta T_{\text{p}}$, $p_4 = p_3$	h_4, s_4
5 (IHX outlet)	h_1, h_2, h_4, p_4	$h_5 = h_4 - (h_2 - h_1)$, $p_5 = p_4$	s_5, T_5
6 (Evaporator inlet)	h_5, p_1	$h_6 = h_5$, $p_6 = p_1$	s_6, T_6
Mass flow (refrigerant)	$\dot{Q}_{\text{sink}}$, h_3, h_4	$\dot{m}_{\text{ref}} = \dot{Q}_{\text{sink}}/(h_3 - h_4)$	—
Enthalpy air evap. out	$\dot{m}_{\text{ref}}$, h_1, h_6, $\dot{m}_{\text{dryer},4}$	$h_{\text{dryer},5} = \dot{m}_{\text{ref}}(h_1 - h_6)/\dot{m}_{\text{dryer},4}$	—

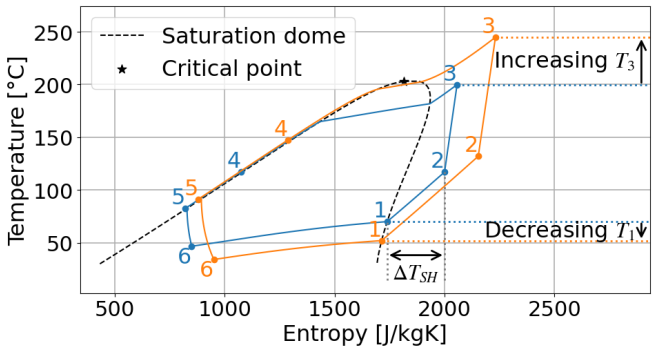

Figure 3.2: Ts diagram illustrating the influence of the pinch temperature on T_1, ΔT_{SH} and T_3.

3.1.2. Degrees of freedom analysis cascade cycle

Table 3.2 summarises the thermodynamic analysis of the cascade heat pump. This analysis shows that the cascade heat pump has three variable temperatures in the upper cycle: the temperature of the working fluid exiting the shared heat exchanger (HEX), T_1; the superheating temperature in the upper cycle, $\Delta T_{\text{SH,u}}$; and the temperature of the working fluid leaving the compressor, T_3. The temperature T_3 is adjusted iteratively to achieve the desired pinch point in the condenser, while $\Delta T_{\text{SH,u}}$ is increased until the pinch point in the IHX is reached. The effects of these temperature adjustments are illustrated in the Ts diagram shown in Figure 3.3a. Since there is no reference point for determining T_1, it will be treated as an optimisation parameter, which will be further explained in section 3.2.2. To demonstrate the simulation process for the upper cycle, the flowchart of the simulation code is presented in Figure B.1 in Appendix B.

In the lower cycle, there are also three variable temperatures: the temperature of the working fluid exiting the evaporator, T_7; the superheating temperature in the lower cycle, $\Delta T_{\text{SH,l}}$; and the temperature of the working fluid leaving the compressor, T_9. The temperatures T_7 and T_9 are adjusted iteratively to achieve the desired pinch point. $\Delta T_{\text{SH,l}}$ is increased iteratively until entropy production no longer decreases or the pinch point in the IHX is reached. The impact of these temperature adjustments is illustrated in the Ts diagram in Figure 3.3b. The flowchart for the lower cycle simulation code is presented in Figure B.2 in Appendix B.

Table 3.2: Summary of the cascade heat pump thermodynamic analysis.

Node / Component	Inputs	Solved	Calculated with REFPROP
Upper cycle			
1 (Evaporator outlet)	T_1, $x_1 = 1$	—	h_1, s_1, p_1
2 (Compressor inlet)	T_1, $\Delta T_{\text{SH,u}}$, p_1	$T_2 = T_1 + \Delta T_{\text{SH,u}}$, $p_2 = p_1$	h_2, s_2
3 (Compressor outlet)	η_{is}, h_2, s_2, T_3	p_3 via iteration on $\eta_{\text{is}} = \dfrac{h_{3s} - h_2}{h_3 - h_2}$	$h_{3s} = h(p_3, s_2)$, h_3, s_3
4 (Condenser outlet)	$T_{\text{air,in}}$, $\Delta T_{\text{p,a}}$, ΔT_{p}, p_3	$T_4 = T_{\text{air,in}} + \Delta T_{\text{p,a}} + \Delta T_{\text{p}}$, $p_4 = p_3$	h_4, s_4
5 (IHX out)	h_1, h_2, h_4, p_4	$h_5 = h_4 - (h_2 - h_1)$, $p_5 = p_4$	s_5, T_5
6 (Evaporator inlet)	h_5, p_1	$h_6 = h_5$, $p_6 = p_1$	s_6, T_6
Upper cycle mass flow	$\dot{Q}_{\text{sink}}$, h_3, h_4	$\dot{m}_{\text{up}} = \dot{Q}_{\text{sink}}/(h_3 - h_4)$	—
Lower cycle			
7 (Evaporator outlet)	T_7, $x_7 = 1$	—	h_7, s_7, p_7
8 (Compressor inlet)	T_7, $\Delta T_{\text{SH,l}}$, p_7	$T_8 = T_7 + \Delta T_{\text{SH,l}}$, $p_8 = p_7$	h_8, s_8
9 (Compressor outlet)	η_{is}, h_8, s_8, T_9	p_9 via iteration on $\eta_{\text{is}} = \dfrac{h_{9s} - h_8}{h_9 - h_8}$	$h_{9s} = h(p_9, s_8)$, h_9, s_9
10 (Condenser outlet)	p_9, T_6, ΔT_{p}	$T_{10} = T_6 + \Delta T_{\text{p}}$, $p_{10} = p_9$	h_{10}, s_{10}
11 (IHX out)	h_7, h_8, h_{10}, p_{10}	$h_{11} = h_{10} - (h_8 - h_7)$, $p_{11} = p_{10}$	s_{11}, T_{11}
12 (Evaporator inlet)	h_{11}, p_7	$h_{12} = h_{11}$, $p_{12} = p_7$	s_{12}, T_{12}
Lower cycle mass flow	h_1, h_6, $\dot{m}_{\text{up}}$, h_9, h_{10}	$\dot{m}_{\text{low}} = \dot{m}_{\text{up}}(h_1 - h_6)/(h_9 - h_{10})$	—
Enthalpy air evap. out	$\dot{m}_{\text{low}}$, h_7, h_{12}, $\dot{m}_{\text{dryer},4}$	$h_{\text{dryer},5} = \dot{m}_{\text{low}}(h_7 - h_{12})/\dot{m}_{\text{dryer},4}$	—

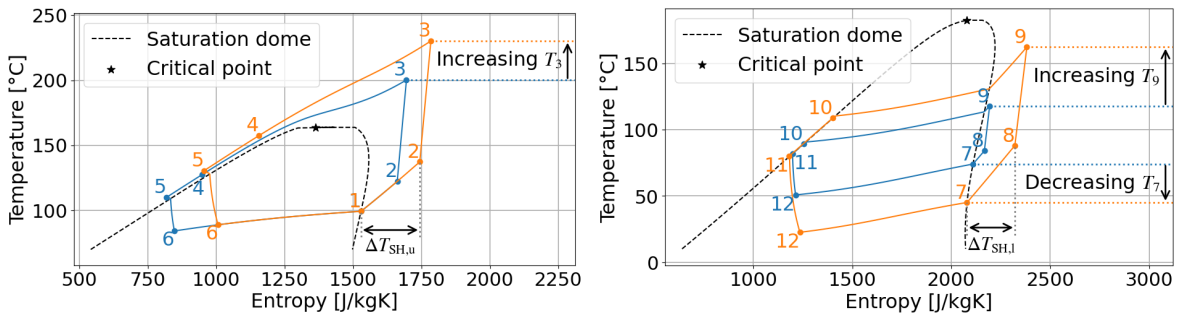

(a) Upper cycle of the cascade heat pump

(b) Lower cycle of the cascade heat pump

Figure 3.3: Ts diagrams illustrating the influence of the pinch temperature in the cascade heat pump on $\Delta T_{\text{SH,u}}$, T_3, T_7, $\Delta T_{\text{SH,l}}$ and T_9.

3.2. Optimisation of the heat pump cycles

The single-stage heat pump optimisation aims to identify the zeotropic mixture or pure fluid with the lowest entropy production. Each of the 78 zeotropic mixtures detailed in Section 2.4 is evaluated to accomplish this. By varying the mole fractions of these mixtures from 0 to 1, the whole range of compositions of the zeotropic mixtures is evaluated.

Optimising the cascade heat pump aims to identify the zeotropic mixtures or pure fluids for the upper and lower cycles that minimise entropy production. The optimisation process should also determine the optimal temperature for the stream exiting the evaporator in the upper cycle, denoted as T_1, as discussed in section 3.1.2. Unlike the single-stage heat pump optimisation, which has only one optimisation variable, the cascade heat pump optimisation involves three variables: the molar fractions of the zeotropic mixtures in both the upper and lower cycles and T_1. The three variables significantly increase the parameter space compared to the one variable in the single-stage optimisation, requiring a more elaborate optimisation logic, which will be explained in Section 3.2.1. Next to the more elaborate optimisation logic, the parameter space is reduced, as will be detailed in Section 3.2.2.

3.2.1. Optimisation logic

The code structure for optimising the single-stage heat pump consists of multiple files, functions, and classes. Figure 3.4 presents a simplified overview of this structure. The optimiser evaluates the heat pump cycle for all 78 mixtures' mole fractions, ranging from 0 to 1 in increments of 0.01, using the `SimpleSingleStage` class. It returns the total entropy production to the optimiser, which then stores the top five mole fractions based on the lowest entropy production values.

Since there can be a slight difference between the mole fraction that yields the lowest entropy production and the one that achieves the highest COP, the optimiser selects the mole fraction with the highest COP from these top five and records it in an Excel file. A more detailed overview of the code structure for optimising the single-stage heat pump can be found in Figure A.2 in Appendix A.

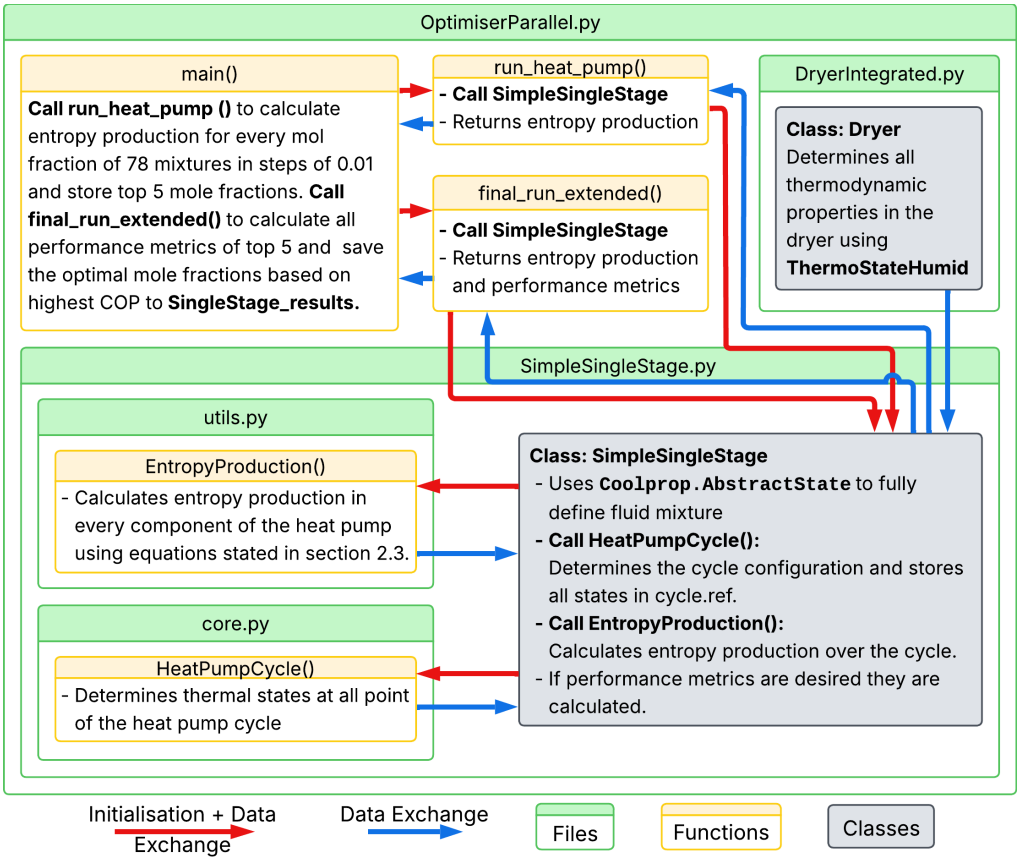

Figure 3.4: Simplified code structure overview of the single-stage heat pump optimisation.

The cascade heat pump optimisation process involves three variables: the mole fractions of the upper and lower cycle, and the temperature at point 1. Determining the optimal heat pump configuration using the single-stage method would require excessive computing power. Therefore, two optimisation functions have been utilised: `skopt.Optimizer` and `SciPy.minimize_scalar`. In optimising the cascade heat pump, `skopt.Optimizer` is used to identify the optimal mole fractions for the upper and lower cycles by employing an algorithm that makes educated guesses about which mole fractions would yield the best performance. The `SciPy.minimize_scalar` function is used to find the optimal temperature T_1. A simplified overview of code structure for the cascade heat pump is shown in Figure 3.5.

For the cascade heat pump optimisation, the top 5 best-performing mole fractions for each cascade pair are saved, and the one with the highest COP is stored in the Excel file. A more detailed overview of the code structure for optimising the cascade heat pump can be found in Figures B.3 and B.4 in Appendix B.

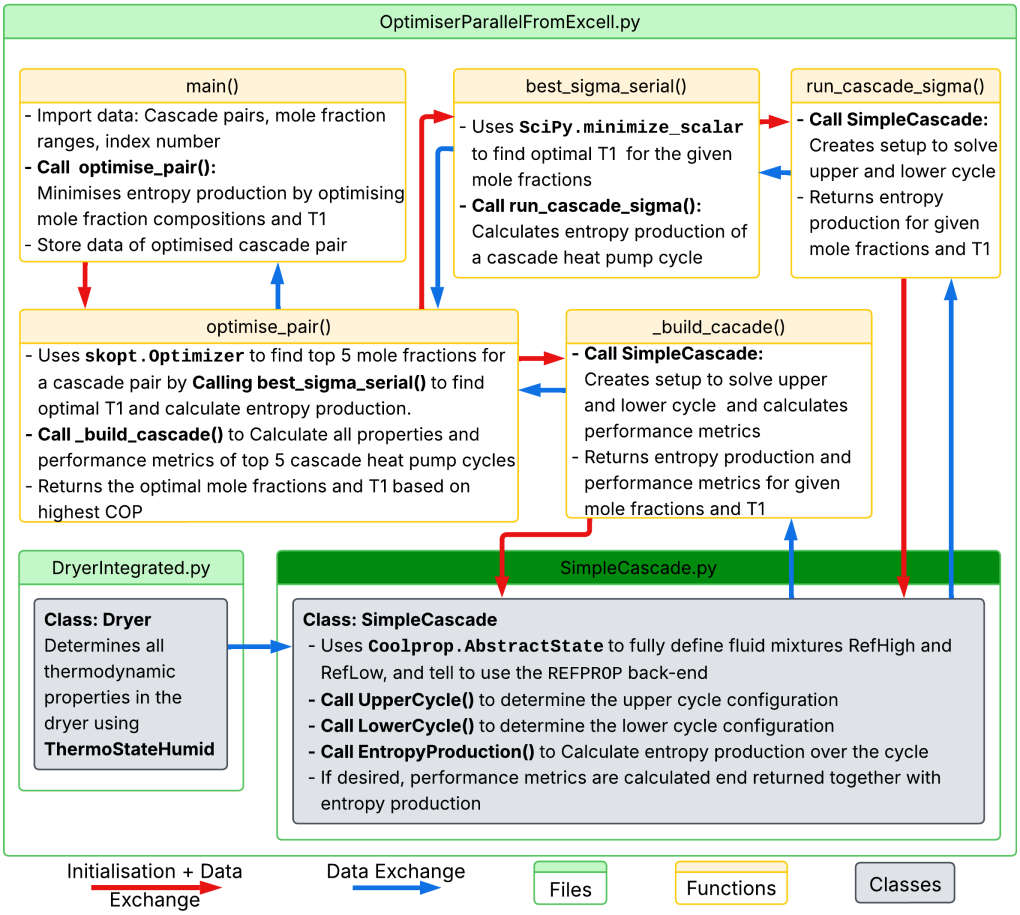

Figure 3.5: Simplified code structure overview of the cascade heat pump optimisation.

3.2.2. Parameter space analysis

For the single-stage heat pump cycle, 78 zeotropic mixtures are analysed. For each binary mixture, 100 different molar fractions are evaluated, resulting in 7800 mixtures for the single-stage heat pump optimisation.

In the cascade heat pump, the same 78 zotropics can be analysed for the upper and lower cycle. With 78 possible mixtures for both cycles, there are 6,084 possible cascade pair combinations (78 x 78). Furthermore, if each mole fraction is assessed in increments of 0.01, the total number of mixture pairs that need to be analysed would be nearly 61 million (6,084 x 100 x 100).

The previous section mentioned one method to reduce the number of mixture evaluations; using the optimisation function `skopt.Optimizer`. However, this approach still leads to an excessive number of mixtures to analyse. To address this problem, the pool of cascade pairs is refined using specific selection criteria.

First, a selection process was conducted for the zeotropic mixtures used in the upper cycle. The upper cycle was simulated for all 78 zeotropic mixtures, with mole fractions ranging from 0 to 1 in increments of 0.01. To select a zeotropic mixture, it had to meet the following requirements:

- A minimum critical temperature of 160 °C to ensure operation near critical or in transcritical conditions, close to the saturation line.
- A maximum working pressure of 50 bar.
- A maximum entropy production of 180 W/K for the compressor, condenser, HEX transferring heat to the sink air, IHX, and expansion valve when solving for the upper cycle at a temperature (T_1) of 90 °C.

These criteria narrowed the pool of potential zeotropic mixtures for the upper cycle down to 10. For the zeotropic mixtures intended for the lower cycle, the following two criteria were established:

- A minimum critical temperature of 110 °C to facilitate subcritical operation.
- A maximum critical pressure of 50 bar.

The selection criteria reduced the pool of zeotropic mixtures for the lower cycle to 42 options. Combined with the pool of zeotropic mixtures for the upper cycle, a total of 420 (10 x 42) cascade pairs remain. To further refine this pool, the complete cycle for each cascade pair was solved with a T_1 of 90 °C. This process was successful for 340 cascade pairs, which now form the final pool for the optimisation routine. Figure 3.6 illustrates a Sankey diagram of the entire selection process.

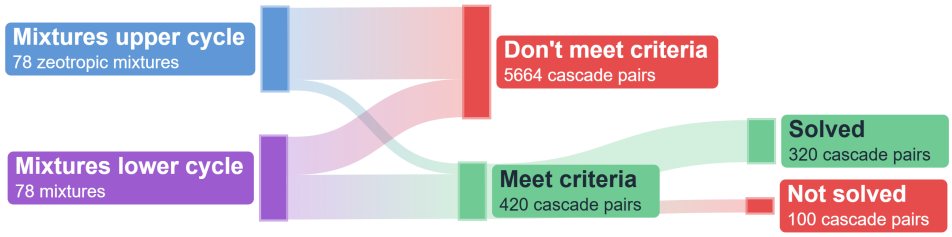

Figure 3.6: Sankey diagram of parameter space reduction for the cascade heat pump optimisation.

The temperature T_1 is optimised using `scipy.minimize_scalar` function, for which it is crucial to specify boundary conditions. Preliminary studies have shown that temperatures below 80 °C lead to a significant difference in pressure ratio between the upper and lower cycles. Conversely, temperatures above 100 °C do not substantially improve entropy production. Therefore, the selected boundary conditions are 80 °C for the lower limit and 100 °C for the upper limit.

3.3. Sizing of heat pump components

This section describes the sizing methods for the compressor and HEXs. First, the simulation of the centrifugal compressor using loss correlations is explained. Following that, the sizing of the brazed plate HEX, which will be used to size the condensers, evaporators, and IHXs, is discussed.

3.3.1. Compressor sizing

The centrifugal compressor has been chosen for the heat pump cycles, as discussed in section 2.5.2. The design approach for estimating the dimensions of the centrifugal compressor and validating the assumed isentropic efficiency is based on widely accepted loss correlations. This methodology is detailed and validated in the work of Uusitalo et al. (2020). The approach involves solving velocity triangles and determining the compressor's main dimensions. The dimensions that remain constant, along with the ratios between them, are presented in Table 3.3. The key dimensions of the impeller are illustrated in Figure 3.7a. Additionally, Table 3.3 provides the velocity ratios necessary to construct the velocity triangle for the impeller. An example of this velocity triangle is shown in Figure 3.7b.

Table 3.3: Input parameters for the design of the compressor that were kept constant

Z	Number of blades	18	Uusitalo et al. (2020)
δ_b	Blade thickness	2 mm	Uusitalo et al. (2020)
t	Tip clearance height	0.5 mm	Uusitalo et al. (2020)
$D_{1,tip}/D_2$	Impeller inlet tip to outlet diameter ratio	0.5	Naukkarinen (2013)
$D_{1,hub}/D_{1,tip}$	Impeller inlet hub-to-tip diameter ratio	0.3	Naukkarinen (2013)
C_{u2}/U_2	Peripheral absolute velocity to peripheral velocity ratio	0.65	Naukkarinen (2013)
C_{r2}/U_2	Radial absolute velocity to peripheral velocity ratio	0.3	Naukkarinen (2013)
D_3/D_2	Diffuser outlet to impeller outlet diameter ratio	1.6	Japiske (1996)
b^*	Diffuser pinch	0.95	Japiske (1996)
e	Relative wake coverage of diffuser passage	0.25	Kus and Nekså (2013)

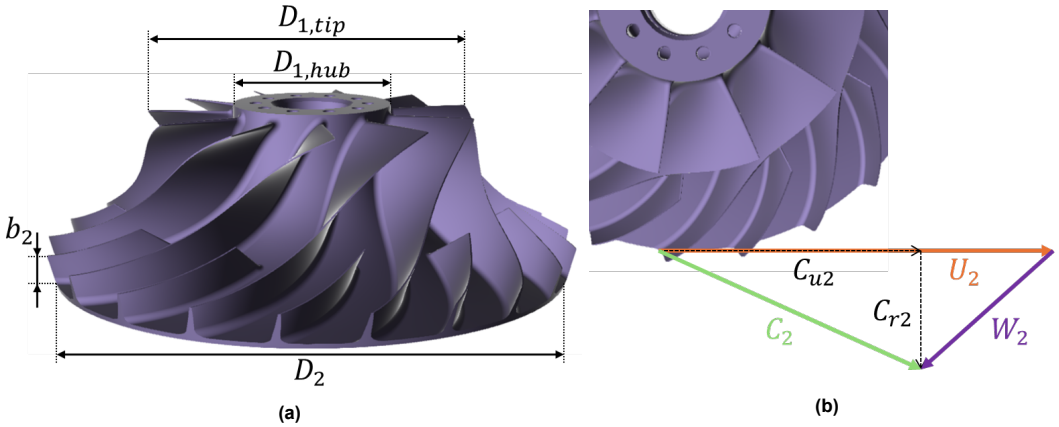

Figure 3.7: Illustrations showing the dimensions of the impeller (a) and the velocity triangle at the impeller outlet (b).

Table 3.4 shows the loss correlations used in this study. It should be noted that this study does not account for leakage losses originating from compressor clearances, except for the tip clearance, nor does it consider potential volute losses.

To determine the optimal compressor design resulting in the highest isentropic efficiency, the specific speed is varied from 0.6 to 1.3. The relationship between the specific speed and the rotational speed of the compressor is given by

$$N_s = \frac{\omega \dot{V}_1^{0.5}}{\Delta h_{is}^{0.75}}, \tag{3.1}$$

where ω represents the rotational speed, $\dot{V}_1$ is the volumetric flow rate at the inlet, and Δh_{is} is the enthalpy difference for isentropic compression. The rotational speed determined for the first stage will be utilised for the subsequent stages, allowing all stages to share a common driving axis.

Utilising the Euler turbomachinery equation and assuming that the flow enters the compressor without pre-swirl, the peripheral velocity at the impeller outlet can be calculated by

$$U_2 = \sqrt{\frac{\Delta h_c}{\chi}}. \tag{3.2}$$

The difference in enthalpy across the compressor, denoted as Δh_c, is initially calculated using an assumed isentropic efficiency of 0.8. After the first iteration, this isentropic efficiency is updated to align with the simulation-determined efficiency, and the simulation is then rerun. This process is iterated until the error between the input isentropic efficiency and the simulated isentropic efficiency falls within a specified threshold.

Table 3.4: Compressor loss correlations

Disk friction	$\Delta h_{\text{df}} = 0.5f(\rho_1 + \rho_2)D_1^2 \frac{U_2^3}{16\dot{m}}$	Daily and Nece (1960)
	where, $Re = \rho_2 U_2 \frac{D_2}{2\mu_2}$	
	$f = 0.0622/Re^{0.2}$	
Tip clearance	$\Delta h_{\text{tc}} = 0.6 \frac{t}{b_2} C_{\text{u2}} \sqrt{2 \frac{\pi}{Z b_2} C_{\text{u2}} C_{\text{r1}} \frac{D_{1,\text{tip}}^2 - D_{1,\text{hub}}^2}{(D_2 - D_{1,\text{tip}})(1+\rho_1/\rho_2)}}$	Jansen (1967)
Skin friction	$\Delta h_{\text{sf}} = 2f \frac{L_b}{D_h} \bar{W}^2$	Jansen (1967)
	where, $f = 0.006$	
	$L_b = \frac{D_{1,\text{tip}}}{2} + D_2 - D_{1,\text{hub}}$	
	$D_h = \pi \frac{D_{1,\text{tip}}^2 - D_{1,\text{hub}}^2}{\pi D_{1,\text{tip}} + 2Z(D_{1,\text{tip}} - D_{1,\text{hub}})}$	
	$\bar{W} = \frac{2W_2 + W_{1,\text{tip}} + W_{1,\text{hub}}}{4}$	
Blade loading	$\Delta h_{\text{bl}} = 0.05 D_f^2 U_2^2$	Coppage and Dallenbach (1956)
	where, $D_f = 1 - \frac{W_2}{W_{1,\text{tip}}} \left(1 + \frac{0.75(U_2 C_{\text{u2}} - U_1 C_{\text{u1}})/U_2^2}{Z/\pi(1 - D_{1,\text{tip}}/D_2) + 2D_{1,\text{tip}}/D_2}\right)$	
Recirculation loss	$\Delta h_{\text{rec}} = 8.0e^{-5} \sinh(3.5\alpha_2^3) D_f^2 U_2^2$	Oh (1999)
Mixing loss	$\Delta h_{\text{mix}} = \frac{1}{1+\tan^2 \alpha_2} \left(\frac{1-e-b^*}{1-e}\right)^2 \frac{C_2^2}{2}$	Johnston and Dean (1966)
Diffuser loss	$\Delta h_{\text{diff}} = 2f \frac{L_{\text{diff}}}{D_{\text{h,diff}}} C_{\text{avg}}^2$	Japiske (1982)
	where, $f = 0.015 \left(\frac{1.8e^5}{Re_{\text{diff}}}\right)^{0.2}$	
	$Re_{\text{diff}} = \frac{\rho C_{\text{r,avg}} D_{\text{h,diff}}}{\mu_2}$	
	$C_{\text{r,avg}} = C_{\text{r2}} \frac{D_2}{2L_{\text{diff}}} \ln \frac{D_3}{D_2} \frac{\rho_2}{0.5(\rho_2 + \rho_3)}$	
	$L_{\text{diff}} = \frac{D_3 - D_2}{2}$	
	$D_{h,\text{diff}} = 2b_2 b^*$	
	$C_{\text{avg}} = \frac{C_2 + C_3}{2}$	

The variable χ represents the ratio of the peripheral absolute velocity to the peripheral velocity (C_{u2}/U_2). Using the peripheral velocity U_2 and the angular velocity ω, the impeller outlet diameter D_2 can be determined. The diameters at the impeller inlet tip and hub, and the velocity triangles can be solved using the ratios provided in Table 3.3. Finally, the outlet blade height b_2 is calculated using continuity equations and the velocity triangles.

The total enthalpy loss is calculated as

$$\Delta h_{\text{loss}} = \Delta h_{\text{df}} + \Delta h_{\text{tc}} + \Delta h_{\text{sf}} + \Delta h_{\text{bl}} + \Delta h_{\text{rec}} + \Delta h_{\text{mix}} + \Delta h_{\text{diff}}, \tag{3.3}$$

which value is then used to calculate the isentropic efficiency per stage as

$$\eta_{\text{is,st}} = \frac{\Delta h_{\text{is}}}{\Delta h_{\text{is}} + \Delta h_{\text{loss}}}. \tag{3.4}$$

The isentropic efficiency for each stage, the pressure ratio per stage, and the initial pressure and temperature are used to determine the overall isentropic efficiency.

The model has been validated using experimental data from Dewar et al. (2019). The design inputs utilised in the experiment are as follows: $\Pi = 2.38$, $\dot{m} = 1.79$ kg/s, $n = 27,660$ rpm, $P_{\text{in}} = 0.96$ bar, $T_{\text{in}} = 300$ K, and $r_3/r_2 = 2$. This data was incorporated into the model, allowing for a comparison of isentropic efficiency and dimensions between the experimental results and the model predictions. The findings are presented in Table 3.5.

Table 3.5: Compressor model validation.

	Fluid	η_{is}, %	D_2, mm	$D_{1,tip}$, mm	$D_{1,hub}$, mm	b_2, mm
Experimental (Dewar et al., 2019)	Air	79.8	270.9	134.9	40.5	12.2
Model	Air	83.4	271.5	135.7	40.7	11.1
Relative difference, %		4.32	0.22	0.59	0.49	-9.91

3.3.2. Heat exchanger sizing

As discussed in section 2.5.1, the condenser/gas cooler, evaporator, and IHXs will all be plate HEXs. Since the pressures in the condenser/gas cooler and IHXs can reach up to 60 bar, a brazed plate HEX has been chosen for these components. To simplify sizing, the evaporator will also be a brazed plate HEX. The HEXs that transfer heat between the HTF and the air will not be simulated. Including them when comparing heat pump configurations is unnecessary, as their sizes remain constant across different heat pump cycles and working fluids.

The results of the sizing of the brazed HEXs will include the following parameters: the length of the plate (L_{pl}), the number of plates (N_{pl}), the total effective heat transfer area (A_{eff}), the mean heat transfer coefficient of the hot fluid ($\alpha_{h,m}$), and the mean heat transfer coefficient of the cold fluid ($\alpha_{c,m}$). To determine these parameters, the plate dimensions must be defined. All required dimensions are shown in Table 3.6. Schematic corrugation and chevron plate drawings are shown in Figure 3.8, indicating the geometrical parameters.

Table 3.6: Input parameters for the design of the HEX that were kept constant

β	Cheveron angle	65°
B	Corrugation depth	2 mm
Λ	Wave lenght of corrugation	5 mm
λ_{pl}	Thermal conductivity plate	17 W/m K
δ_{pl}	thickness of the plate	0.5 mm

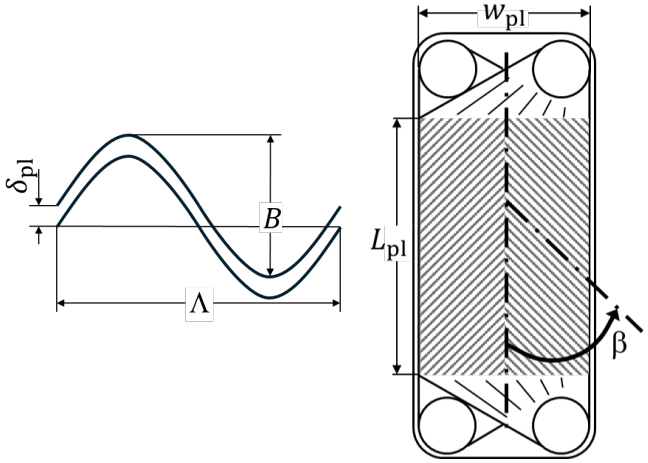

Figure 3.8: Schematic representation of a chevron plate and its geometrical parameters.

Using the dimensions stated in Table 3.6, the hydraulic diameter can be determined as

$$D_h = 2B/\Phi. \tag{3.5}$$

Here B is the corrugation depth and Φ is the area enlargement factor, which can be calculated as

$$\Phi = 1/6\left(1+\sqrt{1+X^2}+4\sqrt{1+X^2/2}\right). \tag{3.6}$$

The area enlargement factor is the ratio of the effective heat transfer area to the projected area. The dimensionless corrugation parameter X that is used to calculate the area enlargement ratio is defined as

$$X = \pi B / \Lambda, \tag{3.7}$$

where Λ is the wavelength of the corrugation.

The heat transfer area can be calculated using the Log Mean Temperature Difference (LMTD) and the overall heat transfer coefficient, as explained in Section 2.5.1. To determine the overall heat transfer coefficient, it is necessary to identify the heat transfer coefficients for both the hot and cold fluids. Calculating these heat transfer coefficients for the different HEXs requires four correlations: one for two-phase condensation of zeotropic mixtures, one for gas cooling, one for two-phase evaporation of zeotropic mixtures, and another for single-phase flow. All correlations are described in Table 3.7.

For the condensation of a zeotropic mixture, an adjusted Silver-Bell-Ghaly method is utilised, as proposed by Zhang et al. (2021a). This method demonstrates strong predictive capabilities, attaining a mean absolute relative error of 12.2% compared to the experimental data for a zeotropic mixture of R134a and R245fa. The heat transfer coefficient for the supercritical fluid in the gas cooler is estimated using the correlation developed by Zendehboudi et al. (2021). This correlation has a mean absolute relative error of 11.6% compared to experimental data for transcritical CO_2. For the evaporation of the zeotropic mixture, the heat transfer coefficient is estimated using a method described by X. Huang et al. (2025), who reported a mean absolute relative error of 11.8% based on experimental data for a propane and isobutane mixture. Finally, the correlation used for the single-phase heat transfer coefficient is proposed by Martin (1996).

To determine realistic HEX sizing, it is essential to consider the pressure drop across the HEX. The total pressure drop can be calculated as

$$\Delta p = \Delta p_{\text{fric}} + \Delta p_{\text{g}} + \Delta p_{\text{acc}}. \tag{3.8}$$

The calculation of each of the terms in Equation (3.8) is detailed in Table 3.8. In the HEX calculation, the pressure drop is maximised at 20 kPa for both the hot and cold streams.

Table 3.7: Heat transfer coefficient correlations for plate heat exchangers

Condensation of zeotropic mixture	
$\frac{1}{\alpha_{\text{tp,cond}}} = \frac{1}{\alpha_{\text{pure}}} + \frac{Z}{\alpha_{\text{V}}}$	Bell and Ghaly (1973)
where, $\alpha_{\text{pure}} = 0.4703 Re_{\text{eq}}^{0.5221} Pr_{\text{L}}^{1/3} Bd^{0.1674} \rho^{*0.2126} (k_{\text{L}}/D_{\text{h}})$	Zhang et al. (2021b)
$\rho^* = \rho_{\text{L}}/\rho_{\text{V}}$	
$Re_{\text{eq}} = \frac{G_{\text{wf}}(1-x_{\text{m}}+x_{\text{m}}\rho^{*0.5})D_{\text{h}}}{\mu_{\text{L}}}$	
$Bd = g(\rho_{\text{L}} - \rho_{\text{V}})D_{\text{h}}^2/\Gamma$	
$Z = x c_{\text{p,v}} \Delta T_{\text{g}}/\Delta h$	Del Col et al. (2005)
$\alpha_{\text{V}} = f_{\text{i}} \alpha_{\text{V}}^0$	Thome et al. (2003)
$\alpha_{\text{V}}^0 = 0.023 Re_{\text{V}}^{0.8} Pr_{\text{V}}^{1/3} (k_{\text{V}}/D_{\text{h}})$	Incropera and Dewitt (1996)
$f_{\text{i}} = 1 + \left(\frac{u_{\text{V}}}{u_{\text{L}}}\right)^{0.5} \left(\frac{(\rho_{\text{L}}-\rho_{\text{V}})g\delta_{\text{film}}}{\Gamma}\right)^{0.25}$	Thome et al. (2003)
$Re_{\text{V}} = \rho_{\text{V}} u_{\text{V}} D_{\text{h}}/\mu_{\text{V}}$	Del Col et al. (2005)
$u_{\text{V}} = \frac{xG}{\rho_{\text{V}}\zeta}$	
$u_{\text{L}} = \frac{(1-x)G}{\rho_{\text{V}}(1-\zeta)}$	
$\delta_{\text{film}} = D_{\text{h}}(1-\zeta)/4$	El Hajal et al. (2003)
$\zeta = \frac{u_{\text{v,s}}}{C_0 u_{\text{m,s}} + C_1 u_{\text{dr}}}$	Zhu and Haglind (2020)
$u_{\text{v,s}} = xG/\rho_{\text{V}}$	
$C_0 = 1.03 \left(\frac{1-x}{x}\right)^{0.02}$	
$u_{\text{m,s}} = G\left(\frac{x}{\rho_{\text{V}}} + \frac{1-x}{\rho_{\text{L}}}\right)$	
$C_1 = 1$ for $\zeta \geq 0.25$, else $C_1 = \left(\frac{1-x}{x}\right)^{0.125}$	
$u_{\text{dr}} = 1.53 \left(\frac{g\Gamma(\rho_{\text{L}}-\rho_{\text{V}})}{\rho_{\text{L}}^2}\right)^{0.25}$	
Cooling of supercritical fluid	
$\alpha_{\text{gc}} = 0.33 Re_{\text{m}}^{0.804} \bar{Pr}_{\text{m}}^{0.1} \left(\frac{\rho_{\text{wall}}}{\rho_{\text{m}}}\right)^{-0.1} \left(\frac{\bar{c}_p}{c_{p,\text{m}}}\right)^{0.093} \left(\frac{Gr}{Re_{\text{m}}^{2.7}}\right)^{0.1}$	Zendehboudi et al. (2021)
$Re_{\text{m}} = GD_h/\mu_{\text{m}}$	
$\bar{Pr}_{\text{m}} = \bar{c}_p \mu_{\text{m}}/\lambda_m$	
$\bar{c}_p = \frac{h_{\text{wall}}-h_{\text{m}}}{T_{\text{wall}}-T_{\text{m}}}$	
$Gr = \frac{(\bar{\rho}_{\text{wall}}-\rho_{\text{m}})\rho_{\text{m}} g D_{\text{h}}^3}{\mu_{\text{m}}^2}$	
$\bar{\rho}_{\text{wall}} = \frac{\int_{T_{\text{wall}}}^{T_{\text{m}}} \rho dT}{T_{\text{m}}-T_{\text{wall}}}$	
Evaporation of zeotropic mixture	
$\alpha_{\text{tp,evap}} = F_{\text{c}} S \alpha_{\text{pool}} + F\alpha_{\text{L}}$	Thome (1996)
where, $F_{\text{c}} = 1 + \frac{\Delta T_g \alpha_{\text{pure}}}{q}\left(1 - exp\left(-\frac{q}{0.0003\rho_{\text{L}}\Delta h}\right)\right)$	Thome (1996)
$\alpha_{\text{pure}} = S\alpha_{\text{pool}} + F\alpha_{\text{L}}$	Zhang and Haglind (2021)
$S = 1/\left(1 + 2.53e^{-6}\left(Re_{\text{L}} F^{1.25}\right)^{1.17}\right)$	Chen (1966)
$F = 2.35(X_{tt}^{-1} + 0.213)^{0.736}$	Chen (1966)
$X_{tt} = \left(\frac{\rho_{\text{V}}}{\rho_{\text{L}}}\right)^{0.5} \left(\frac{\mu_{\text{L}}}{\mu_{\text{V}}}\right)^{0.1} \left(\frac{1-x}{x}\right)^{0.9}$	
$\alpha_{\text{pool}} = \alpha_{\text{cooper}} = 35 P_r^{0.12} (-\log_{10} P_r)^{-0.55} M^{-0.5} (q/1000)^{0.67}$	Cooper (1989)
$\alpha_{\text{L}} = 0.023 Re_{\text{L}}^{0.8} Pr_{\text{L}}^{1/3}$	Incropera and Dewitt (1996)
Single-phase heating and cooling	
$\alpha_{\text{sp}} = 0.122 Pr^{1/3} \left(\frac{\mu_{\text{avg}}}{\mu_{\text{wall}}}\right)^{1/6} (fRe^2 sin2\beta)^{0.374}$	Martin (1996)
$f = \left(\frac{cos\beta}{(0.18tan\beta + 0.36sin\beta + f_0/cos\beta)^{0.5}} + \frac{1-cos\beta}{3.8 f_1^{0.5}}\right)^{-2}$	
$f_0 = \begin{cases} 64/Re & Re < 2000 \\ (1.8\log_{10} Re - 1.5)^{-2}, & Re \geq 2000 \end{cases}$	
$f_1 = \begin{cases} 579/Re + 3.85, & Re < 2000 \\ 39/Re^{0.289}, & Re \geq 2000 \end{cases}$	

Table 3.8: Pressure drop calculations in cheveron plate heat exchanger.

Friction	$\Delta p_{\text{fric}} = 2f\frac{G^2}{\rho}\frac{L_{\text{pl}}}{D_h}$	
	Fanning friction factor condensation zeotropic mixture	
	$f = (4.207 - 2.673\beta^{-0.46})(4200 - 5.41Bd^{1.2})Re_{\text{eq}}^{-0.95}(p_{\text{sat}}/p_{\text{crit}})^{0.3}$	Tao and Infante Ferreira (2019)
	$Re_{\text{eq}} = G * (1 - x + x(\rho_{\text{L}}/\rho_{\text{V}})^{0.5})D_h/\mu_{\text{L}}$	
	$Bd = (\rho_{\text{L}} - \rho_{\text{V}})gD_h^2/\Gamma$	
	Fanning friction factor evapaoration zeotropic mixture	
	$f = \begin{cases} 0.2090Re_{\text{eq}}^{0.6043}Re_{\text{L}}^{0.6043} & Re < 6000 \\ 0.2090Re_{\text{eq}}^{0.0672}Re_{\text{L}}^{0.7279}, & Re \geq 6000 \end{cases}$	Yan and Lin (1999)
	$Re_{\text{L}} = GD_h/\mu_{\text{L}}$	
	Fanning friction factor single-phase	
	$f = \frac{1}{4}\left(\frac{cos\beta}{(0.18tan\beta + 0.36sin\beta + f_0/cos\beta)^{0.5}} + \frac{1-cos\beta}{3.8f_1^{0.5}}\right)^{-2}$	Martin (1996)
	$f_0 = \begin{cases} 64/Re & Re < 2000 \\ (1.8\log_{10}Re - 1.5)^{-2}, & Re \geq 2000 \end{cases}$	
	$f_1 = \begin{cases} 579/Re + 3.85, & Re < 2000 \\ 39/Re^{0.289}, & Re \geq 2000 \end{cases}$	
Acceleration	$\Delta p_{\text{acc}} = G^2(x_{\text{in}} - x_{\text{out}})(1/\rho_{\text{V}} - 1/\rho_{\text{L}})$	X. Huang et al. (2025)
Gravitational	$\Delta p_{\text{g}} = \begin{cases} -gL_{\text{pl}}(\rho_{\text{in}} - \rho_{\text{out}})/2, & \text{if fluid enters at the top} \\ gL_{\text{pl}}(\rho_{\text{in}} - \rho_{\text{out}})/2, & \text{if fluid enters at the bottom} \end{cases}$	X. Huang et al. (2025)

4

Results

This chapter presents the results of the optimisations performed on single-stage and cascade heat pumps. For both heat pump types, two refrigerant mixtures or cascade pairs are selected for a more in-depth evaluation. The compressors and heat exchangers for these mixtures and cascade pairs are sized, and the results are presented. The final section of this chapter presents a sensitivity analysis, examining the impact of the internal heat exchanger (IHX), heat transfer fluid (HTF), energy losses i the dryer, and the dryer's dew point temperature on the heat pump's performance.

4.1. Single-stage heat pump

The single-stage heat pump optimiser evaluated 78 different mixtures and successfully identified solutions for 69 of them. Among these 69 mixtures, the pure fluid performed best in 4 cases. To ensure the accuracy of the entropy calculations, the COP was computed using both Equation (2.2) and Equation (2.10). The COP values obtained from both calculations were identical, confirming that the entropy production calculations were accurate.

The optimisation results are shown in Figure 4.1, where each point represents the optimal composition for each of the 69 mixtures evaluated. The mixtures are categorised based on their dominant component. As mentioned earlier, four of these points correspond to pure fluids: one for ammonia, one for butane, and two for hexane. The pure fluids are indicated with squares in Figure 4.1, which shows that pure fluids exhibit the lowest COP among their respective groups. The graph illustrates a Pareto front, suggesting no absolute optimal point exists; instead, trade-offs must be carefully considered.

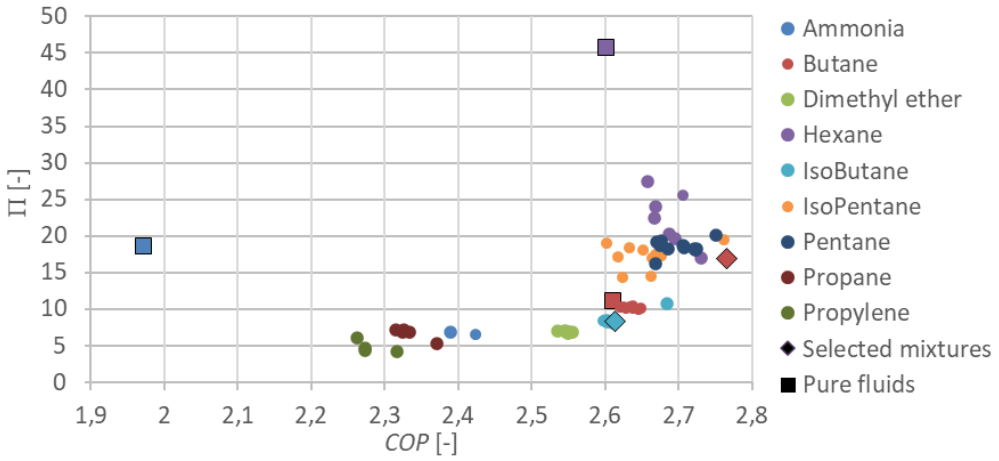

Figure 4.1: Scatter diagram of the single-stage heat pump optimisation results showing the COP vs Π for the optimal composition of each mixture. The colour of the dots indicates the mixture's dominant component (> 50 mol%). The squares in the diagram represent pure fluids, and diamonds represent the mixtures selected for further analysis.

The mixture consisting of 51 mol% butane and 49 mol% hexane exhibits the highest performance, achieving a COP of 2.77. As indicated by the red diamond in Figure 4.5, this mixture has a relatively high pressure ratio (Π) of 16.89. Figure 4.2 illustrates the Ts and TQ diagrams for this cycle, which demonstrates that it operates in the subcritical region.

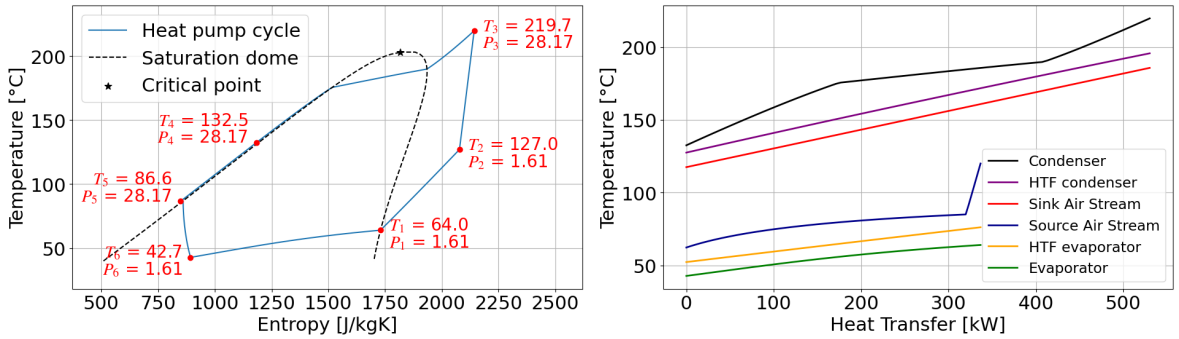

Figure 4.2: Ts (left) and TQ (right) diagrams for 51 mol% butane & hexane with COP = 2.77 and Π = 16.89.

To compare the butane-hexane mixture with another mixture that requires a lower pressure ratio, the mixture composed of 96 mol% isobutane and 4 mol% propylene is selected, indicated with the light blue diamond in Figure 4.5. This mixture achieves a COP of 2.61 and has a pressure ratio of 8.13. Figure 4.3 displays the Ts and TQ diagrams for this mixture, which indicate that this cycle operates in the transcritical region.

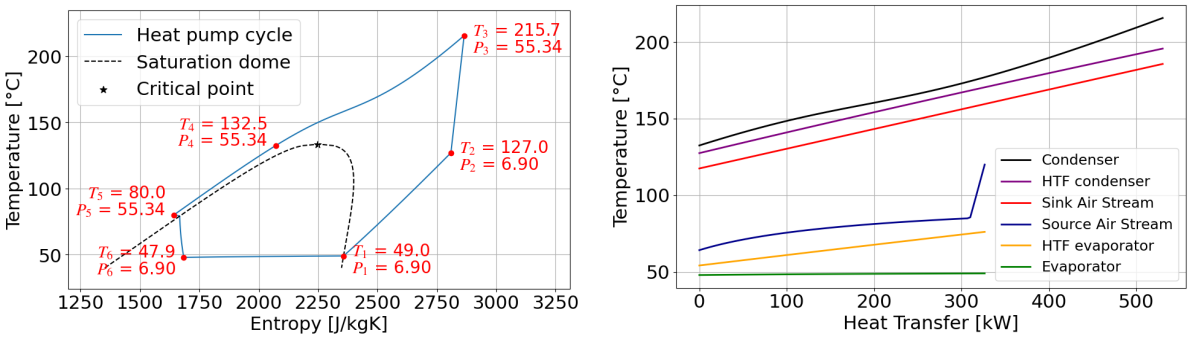

Figure 4.3: Ts (left) and TQ (right) diagrams for 96 mol% isobutane & propylene with COP = 2.61 and Π = 8.13.

The two cycles can be compared based on the entropy production in each of their components, as illustrated in Figure 4.4. The isobutane-propylene mixture performs better than the butane-hexane mixture in the condenser; however, the butane-hexane mixture outperforms the isobutane-propylene mixture in the evaporator. This variation in performance can be attributed to glide matching. The TQ diagrams shown in Figures 4.2 and 4.3 show better glide matching for the isobutane-propylenen mixture in the condenser, while in the evaporator, the glide matching is better for the butane-hexane mixture.

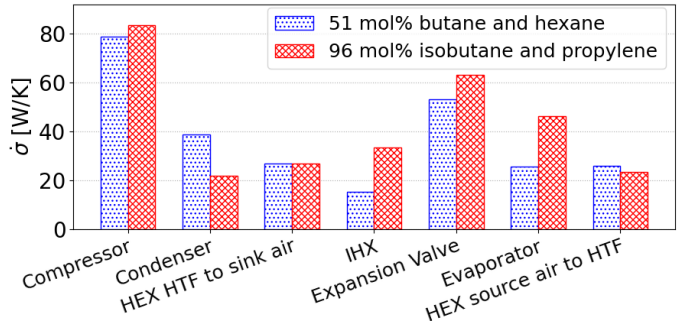

Figure 4.4: Bar diagram showing the entropy production of each component in the single-stage heat pump cycles.

The poorer performance of the isobutane-propylene mixture is not due to higher entropy production in the evaporator, as this is offset by improved performance in the condenser. Instead, the significant performance difference compared to the butane-hexane mixture is primarily due to increased entropy production in the IHX and the expansion valve. In the IHX, higher entropy production occurs partly because the high-pressure fluid can be cooled to a lower temperature, since the working fluid exiting the evaporator is at a lower temperature than the butane-hexane mixture. At the same time, the lower inlet temperature to the expansion valve helps reduce the entropy production across it. However, the overall entropy production across the expansion valve is still higher for the isobutane-propylene mixture. The higher entropy production suggests that the transcritical cycle may perform worse than the subcritical cycle because the expansion process begins farther from the two-phase region.

4.1.1. Sizing of the single-stage heat pump components

To compare the butane-hexane mixture with the isobutane-propylene mixture on a component basis, the HEXs and compressors have been sized. The results of the compressor sizing are detailed in Table 4.1. Both mixtures require small, fast-spinning impellers to achieve the desired pressure ratios. Although the butane-hexane mixture demonstrates better peformance when assuming an isentropic compressor efficiency of 80%, the adjusted COP based on the simulated compressor power input is greater for the isobutane-propylene mixture. To calculate the adjusted COP shown in Table 4.1, the total heat output of the heat pump of 530 kWth was divided by the power input found by simulating the compressor.

Table 4.1: This table shows the sizing and performance of 2-stage and 3-stage centrifugal compressors for 51 mol% butane & hexane and 96 mol% isobutane & propylene mixtures. Abbreviations are defined in section 3.3.1. The adjusted COP is calculated by dividing the heat pump's total output of 530 kWth by the compressors' power input from the simulation.

	51 mol% butane & hexane		96 mol% isobutane & propylene	
Number of compressor stages	2 stages	3 stages	2 stages	3 stages
P_{c}, kW	219.35	210.86	208.72	207.26
η_{is}, %	69.8	72.6	77.8	78.4
n, krpm	86	64	102	82
Adjusted COP, $-$	2.42	2.52	2.54	2.56
Π_{stage}, $-$	4.11	2.57	2.85	2.01
1st compressor stage				
$P_{\text{c,st}}$, kW	111.86	71.97	107.03	71.59
$\eta_{\text{is,st}}$, %	70.7	73.2	78.8	78.8
D_2, mm	82.7	89.6	61.9	62.8
$D_{1,\text{tip}}$, mm	41.4	44.8	31.0	31.4
$D_{1,\text{hub}}$, mm	12.4	13.4	9.3	9.4
b_2, mm	3.5	6.3	3.5	5.2
2nd compressor stage				
$P_{\text{c,st}}$, kW	107.49	65.86	101.69	68.82
$\eta_{\text{is,st}}$, %	72.1	81.4	79.2	81.4
D_2, mm	80.6	85.5	60.1	61.7
$D_{1,\text{tip}}$, mm	40.3	42.8	30.1	30.8
$D_{1,\text{hub}}$, mm	12.1	12.8	9.0	9.3
b_2, mm	1.4	3.8	1.8	2.9
3rd compressor stage				
$P_{\text{c,st}}$, kW	-	73.03	-	66.85
$\eta_{\text{is,st}}$, %	-	69.0	-	79.3
D_2, mm	-	89.6	-	60.4
$D_{1,\text{tip}}$, mm	-	44.8	-	30.2
$D_{1,\text{hub}}$, mm	-	13.4	-	9.1
b_2, mm	-	1.2	-	1.8

The results of the sizing of the HEXs are detailed in Table 4.2. The gas cooler for the isobutane-propylene mixture has a heat transfer area that is 111% larger than that of the butane-hexane condenser. Conversely, the evaporator for the butane-hexane mixture is 104% larger than that for the isobutane-propylene mixture. These differences can be partly attributed to glide matching; better glide matching results in a smaller LMTD, which necessitates a larger heat transfer area.

Table 4.2: Sizing of the brazed plate heat exchangers for the 51 mol% Butane & Hexane and 96 mol% Isobutane & Propylene mixtures. The abbreviations used in the table are explained in section 3.3.2.

51 mol% Butane & Hexane	L_{pl} (m)	w_{pl} (m)	N_{pl} $(-)$	A_{eff} (m^2)	$\alpha_{h,m}$ (kW/m^{2}K)	$\alpha_{c,m}$ (kW/m^{2}K)
Condenser	1.228	0.5	55	45	2.55	1.75
Evaporator	0.546	0.25	257	47	1.59	4.40
IHX	0.385	0.2	215	22	1.16	1.31
96 mol% Isobutane & Propylene						
Gas cooler	1.496	0.5	95	95	1.95	1.34
Evaporator	0.544	0.25	129	23	2.29	5.94
IHX	0.427	0.2	141	16	2.03	2.11

4.2. Cascade heat pump

The cascade heat pump optimiser evaluated 340 mixtures and found a solution for each. A pure fluid outperformed mixtures in the lower cycles four times, but never in the upper cycle. The COP was calculated using both Equations (2.2) and (2.10), yielding identical values and confirming the accuracy of the entropy production calculations.

The results of the cascade heat pump optimisation are presented in Figure 4.5. This figure shows that, unlike single-stage heat pumps, high-performing cascade pairs are identified at low pressure ratios. The most efficient cascade cycle consists of a mixture of 61 mol% isopentane and 39 mol% dimethyl ether in the upper cycle, and a mixture of 74 mol% butane and 26 mol% hexane in the lower cycle. This combination will be referred to as cascade pair 1, which is marked with a yellow diamond in Figure 4.5. Cascade pair 1 operates at a pressure ratio of 5.00 in the upper cycle and 2.98 in the lower cycle, achieving a COP of 2.68. The Ts diagrams for cascade pair 1, shown in Figure 4.6, indicate that the upper cycle is transcritical while the lower cycle is subcritical.

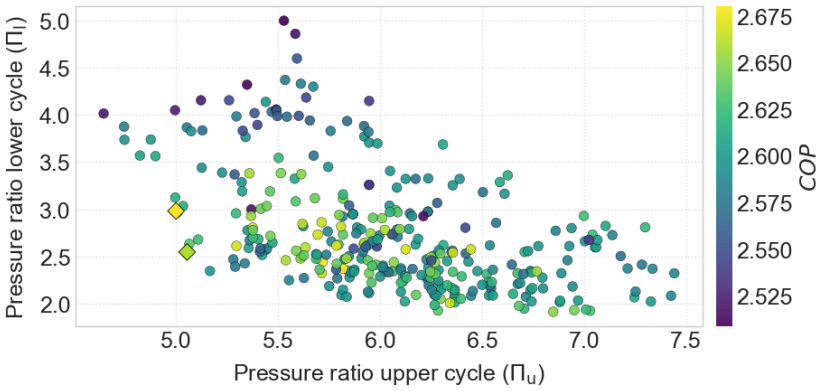

Figure 4.5: Scatter diagram of the cascade heat pump optimisation results displaying the pressure ratios for the upper (Π_u) and lower (Π_l) cycles on the x-axis and y-axis. The colour of each point indicates the corresponding COP value, and the diamonds represent the selected cascade pairs for further analysis.

To compare the performance of cascade pair 1 with another, cascade pair 2 is selected, which consists of a upper cycle mixture of 55 mol% isopentane and 45 mol% dimethyl ether, and a lower cycle mixture composed of 62 mol% dimethyl ether and 38 mol% isopentane. This cascade pair is represented by a green diamond in Figure 4.5. Cascade pair 2 operates at a pressure ratio of 5.05 in the upper cycle and 2.55 in the lower cycle, achieving a COP of 2.66. For clarity, the mixtures used in both cascade pairs are described in Table 4.3.

Table 4.3: Description of the compositions of cascade pairs 1 and 2

	Working fluid upper cycle	Working fluid lower cycle
Cascade pair 1	61 mol% isopentane & dimethyl ether	74 mol% butane & hexane
Cascade pair 2	55 mol% isopentane & dimethyl ether	62 mol% dimethyl ether & isopentane

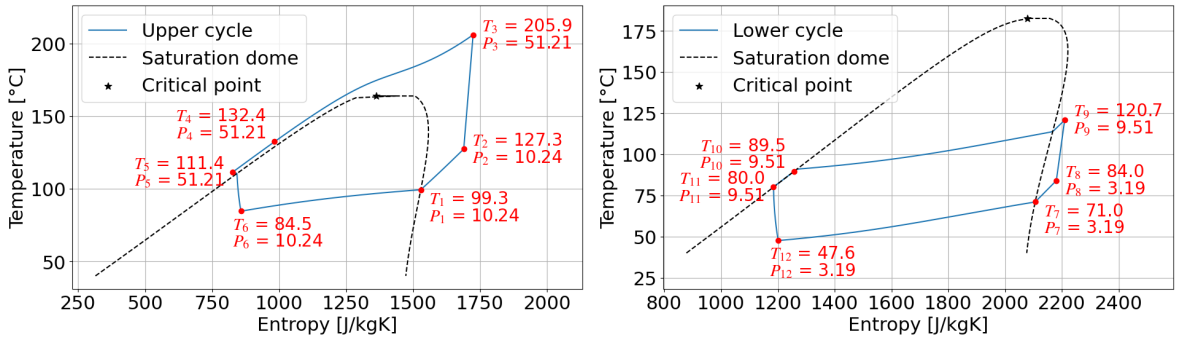

(a) Ts diagram of the upper cycle: 61 mol% isopentane and dimethyl ether with Π = 5.00.

(b) Ts diagram of the lower cycle: 74 mol% butane and hexane with Π = 2.98.

Figure 4.6: Ts diagrams of cascade pair 1 with a COP of 2.68.

The two cascade pairs can be analysed based on the entropy production in each component of the cascade heat pump, as illustrated in Figure 4.7. The results reveal minimal differences between the two cycles. The entropy production in both the condenser and evaporator indicates effective glide matching, as the entropy production for both cascade pairs is comparable to that of the condenser in the single-stage heat pump using the isobutane-propylane mixture, and to the evaporator of the single-stage heat pump employing the butane-hexane mixture. However, the better overall glide matching of the cascade heat pump is offset by entropy production in the shared HEX, which prevents it from significantly outperforming the single-stage heat pump.

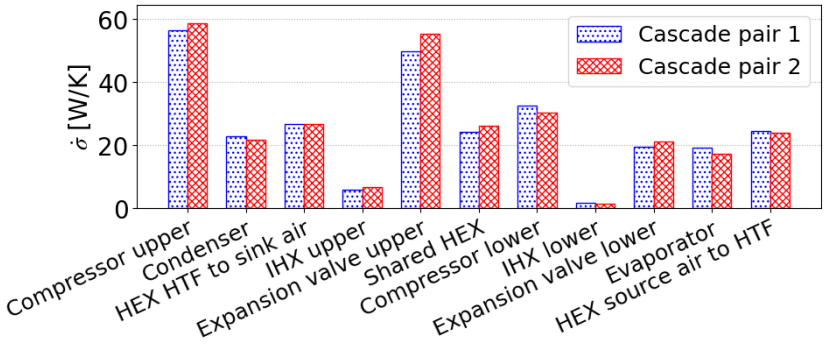

Figure 4.7: Bar diagram showing the entropy production in the cascade heat pump cycles with cascade pair 1 and 2.

4.2.1. Sizing of the cascade heat pump components

To compare the two cascade pairs on a component basis, the HEXs and compressors have been sized. The sizing and performance details for the compressors in both the upper and lower cycles of the cascaded pairs are presented in Table 4.4. Similar to single-stage heat pumps, fast-spinning, small impellers are required to achieve the desired pressure ratio. The adjusted COP for cascade pair 1, when using a single-stage compressor for both the upper and lower cycles, is 2.65. Switching to a two-stage compressor for both cycles increases the adjusted COP by 0.9%. For cascade pair 2, utilising a two-stage compressor in both cycles results in an adjusted COP of 2.64. Therefore, after accounting for simulated compressor efficiency, cascade pair 1 still outperforms cascade pair 2.

The sizing of HEXs is detailed in Table 4.5. The sizes of the HEXs for both cascade pairs differ little. The total heat transfer area of all HEXs combined is 216 m² for cascade pair 1 and 211 m² for cascade pair 2. The most significant difference between the two heat pump cycles lies in the Gas cooler and the shared HEX. The gas cooler for cascade pair 2 is 4.9% larger, while the shared HEX in cascade pair 1 is 17.9% larger.

Table 4.4: This table shows the sizing and performance of 1-stage and 2-stage centrifugal compressors for cascade pairs 1 and 2. Abbreviations are defined in section 3.3.1. The adjusted COP is calculated by dividing the heat pump's total output of 530 kWth by the compressors' power input from the simulation.

	Cascade pair 1				Cascade pair 2			
	Upper cycle		Lower cycle		Upper cycle		Lower cycle	
Number of compressor stages	1 stage	2 stages	1 stage	2 stages	1 stage	2 stages	1 stage	2 stages
P_c, kW	137.04	136.87	63.10	61.52	144.92	142.06	60.78	58,68
η_{is}, %	78.5	78.6	80.5	82.6	77.1	78.6	78.7	81.5
n, krpm	125	84	61	39	137	88	86	54
Π_{stage}, $-$	5.00	2.24	2.98	1.73	5.05	2.25	2.55	1.60
1st compressor stage								
$P_{c,st}$, kW	137.04	72.87	63.10	30.67	144.92	75.12	60.78	29.30
$\eta_{is,st}$, %	78.5	79.4	80.5	83.4	77.1	79.3	78.7	82.4
D_2, mm	55.4	59.7	93.1	101.9	51.9	57.9	63.7	71.6
$D_{1,tip}$, mm	27.7	29.8	46.5	51.0	26.0	29.0	31.9	35.8
$D_{1,hub}$, mm	8.3	8.9	14.0	15.3	7.8	9.3	9.6	10.7
b_2, mm	2.3	3.0	3.3	6.0	2.1	3.0	2.4	4.4
2nd compressor stage								
$P_{c,st}$, kW	-	64.0	-	30.85	-	66.94	-	29.38
$\eta_{is,st}$, %	-	79.9	-	82.5	-	80.2	-	81.6
D_2, mm	-	56.1	-	102.3	-	55.0	-	71.7
$D_{1,tip}$, mm	-	28.0	-	51.2	-	27.5	-	35.8
$D_{1,hub}$, mm	-	8.4	-	15.3	-	8.2	-	10.8
b_2, mm	-	2.0	-	3.4	-	2.0	-	2.7

Table 4.5: Sizing of the brazed plate heat exchangers for cascade pair 1 and cascade pair 2. The abbreviations used in the table are explained in section 3.3.2.

Cascade pair 1	L_{pl} (m)	w_{pl} (m)	N_{pl} $(-)$	A_{eff} (m^2)	$\alpha_{h,m}$ (kW/m^{2}K)	$\alpha_{c,m}$ (kW/m^{2}K)
Gas cooler	1,491	0,5	89	88	2.12	1.38
IHX upper	0.318	0.2	103	9	2.98	2.88
shared HEX	0.886	0.4	115	54	2.61	4.45
IHX lower	0.180	0.1	185	4	1.71	2.14
Evaporator	0.885	0.4	131	61	1.83	4.05
Cascade pair 2						
Gas cooler	1.498	0.5	93	92	2.08	1.35
IHX upper	0.324	0.2	101	9	3.05	2.88
shared HEX	0.930	0.4	93	46	2.54	5.29
IHX lower	0.131	0.1	109	2	3.66	3.04
Evaporator	1.189	0.4	99	62	2.12	4.20

4.3. Comparison between the single-stage and cascade cycles

To assess the performance of various heat pump cycles and determine the optimal choice, key data from the two single-stage heat pump mixtures and the two cascade pairs are compiled in Table 4.6. A two-stage compressor is used for the single-stage heat pump and the upper cycle of the cascade heat pump, while a single-stage compressor is used for the lower cycle in the cascade heat pump.

In Table 4.6, the best-performing values are highlighted in bold. The highlighted values show that, after adjusting for compressor performance, a higher COP can be achieved with a cascade heat pump cycle. Specifically, cascade pair 1 shows an improvement of 4.3% in COP compared to the single-stage heat pump cycle using the isobutane-propylene mixture. However, this enhancement may not be sufficient to justify the higher capital costs of transitioning from a single-stage to a cascade heat pump system, as it requires adding a single-stage compressor and two HEXs.

Table 4.6: This table summarises the key performance indicators and dimensions for the heat pump cycles in sections 4.1 and 4.2. The single-stage cycles use a two-stage centrifugal compressor, while the cascade cycles feature a two-stage compressor in the upper cycle and a single-stage compressor in the lower cycle.

	Single-stage heat pump		Cascade heat pump	
	51 mol% butane and hexane	96 mol% isobutane and propylene	Cascade pair 1 (upper / lower)	Cascade pair 2 (upper / lower)
Adjusted COP, $-$	2.42	2.54	**2.65**	2.61
Π_{stage}, $-$	4.11	2.85	**2.24 / 2.98**	2.25 / 2.55
n, krpm	86	102	**84 / 61**	88 / 86
η_{is} compressor, %	69.8	77.8	**78.6 / 80.5**	78.6 / 78.7
D_2 impeller stage 1, mm	82.7	61.9	59.7 / 93.1	57.9 / 63.7
D_2 impeller stage 2, mm	72.1	60.1	56.1 / -	55.0 / -
Total HEX area, m^2	**114**	134	216	211

4.4. Sensitivity study

As discussed in the previous section, the improvement in the COP of the cascade heat pump may not justify the increased capital costs. Therefore, this section focuses on a sensitivity study of single-stage heat pump cycles, specifically examining the effects of the IHX, the HTF, energy losses in the dryer, and the dryer's dew point temperature on the heat pump's performance.

The effects of the IHX are analysed to determine their importance for optimal performance. Additionally, the impact of the HTF on performance is examined, as an HTF is required only when the heat pump is located in a secluded area. To analyse the effects of the IHX and HTF, various configurations of the single-stage heat pump were simulated using butane-hexane and isobutane-propylene mixtures. The results of these simulations are summarised in Table 4.7. Comparing cycles with and without an IHX shows that including an IHX leads to an average COP increase of 45.53% for cycles utilising an HTF and 34.74% for cycles that do not. Furthermore, evaluating cycles with and without an HTF, the COP increases by 5.72% for cycles equipped with an IHX, and by 14.29% for those without an IHX.

Table 4.7: Performance comparison for different IHX and HTF configurations (✓ = used, ✗ = not used).

	✓ IHX	✓ HTF	✓ IHX	✗ HTF	✗ IHX	✓ HTF	✗ IHX	✗ HTF
Fluid mixture	COP	η_{II} (%)	COP	η_{II} (%)	COP	η_{II} (%)	COP	η_{II} (%)
51 mol% butane & hexane	2.766	52.24	2.917	55.42	1.870	33.86	2.220	40.96
96 mol% isobutane & propylene	2.611	49.03	2.767	52.28	1.824	32.95	2.004	36.59

Most studies on implementing a heat pump in drying processes assume isenthalpic drying; however, this study considers an energy loss of 20% of the total heat input. To analyse the impact of this assumption, the effect of energy losses within the dryer is investigated. By varying energy losses from 0% to 30% of the total heat input and simulating the heat pump cycles, the influence of these dryer losses on heat pump performance can be assessed.

Figure 4.8a presents the results of the simulations conducted. When comparing the COP at 20% dryer losses to the isenthalpic drying scenario (0% dryer losses), there is a notable improvement of 3.2% for the butane-hexane mixture and 5.9% for the isobutane-propylene mixture.

In addition to decreasing energy losses in the dryer, increasing the dew point temperature of the humid air exiting the dryer can also improve the COP, as shown in Figure 4.8b. Specifically, increasing the dew point temperature from 85 °C to 90 °C results in a 4.8% improvement in COP for the butane-hexane mixture and a 2.9% improvement for the isobutane-propylene mixture.

It can be concluded that reducing energy losses in the dryer and increasing dew point temperatures can enhance the COP. To explore whether a combination of higher dew points and reduced energy losses can further improve the COP, simulations were conducted for the single-stage heat pump cycles with dew points ranging from 80 °C to 90 °C and dryer losses varying from 0% to 30%. The results of these simulations are presented in Figures 4.8c and 4.8d.

Reducing dryer losses from 20% to 0% while increasing the dew point from 85 °C to 90 °C leads to a 7.4% increase in the COP for a butane-hexane mixture and an 11.6% increase for an isobutane-propylene mixture. The most significant rise in COP occurs when energy losses drop from 30% to 20%, resulting in an average increase of 7.5% in COP across various dew points for both mixtures. Furthermore, raising the dew point from 80 °C to 90 °C yields an average COP increase of 8.0% across the four different levels of energy loss simulated for both mixtures. This substantial performance improvement, resulting from reduced energy losses and increased dew point, demonstrates that achieving a higher COP involves not only optimising the heat pump cycle but also optimising the dryer.

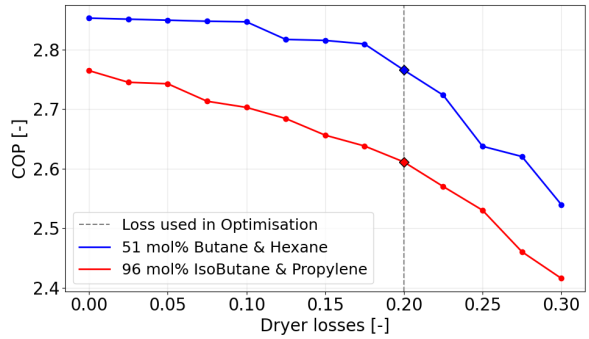

(a) Impact of losses in the dryer on the COP of a single-stage heat pump with a θ_{dp} of 85 °C in the dryer.

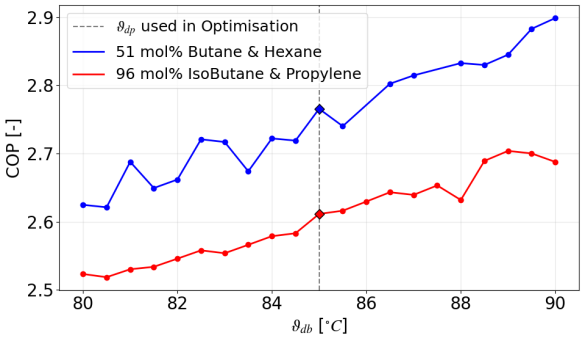

(b) Impact of dew point temperature in the dryer on the COP of a single-stage heat pump with a loss of 20% in the dryer.

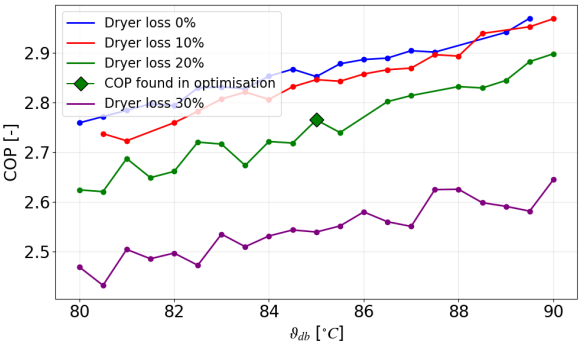

(c) Impact of dryer losses and dew point on COP for a single-stage heatpump with 51 mol% butane & hexane.

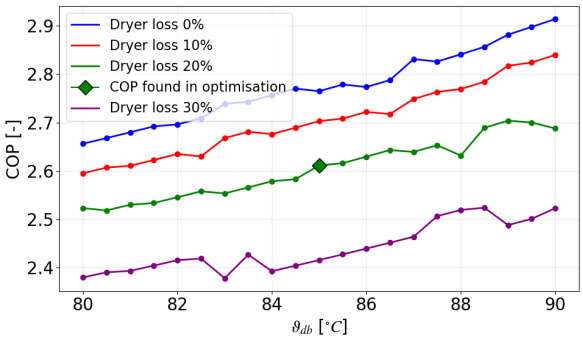

(d) Impact of dryer losses and dew point on COP for a single-stage heatpump with 96 mol% isobutane & propylene.

Figure 4.8: Influence of dryer losses and dew point temperature in the dryer on heat pump performance.

5

Conclusion and discussion

This thesis focused on designing and optimising a heat pump cycle for integration into an industrial dryer. Two heat pump cycles were simulated and optimised using different zeotropic mixtures and adjusting their molar fractions. The compressors and heat exchangers were sized to compare the various heat pump cycles on a component-by-component basis.

The highest COP was observed in a single-stage heat pump cycle utilising a zeotropic mixture of 51 mol% butane and 49 mol% hexane, operating subcritically. This mixture was compared to another well-performing zeotropic mixture, consisting of 96 mol% isobutane and 4 mol% propylene, operating transcritically, which exhibited a significantly lower pressure ratio in the compressor. In the optimisation, where an isentropic efficiency of 80% for the compressor was assumed, the isobutane-propylene mixture recorded a 5.6% lower COP than the butane-hexane mixture. However, upon evaluating the compressor performance of both mixtures, it was found that the adjusted COP for the isobutane-propylene mixture was 5.1% higher than the butane-hexane mixture when employing a two-stage centrifugal compressor for both mixtures. The significant reduction in the COP for the butane and hexane mixture can be attributed to the required pressure ratio. A higher pressure ratio demands greater tip velocities, which in turn result in increased losses. While a higher pressure ratio can lead to increased COP, as demonstrated in Figure 4.1, this principle does not hold true when considering compressor efficiency. Consequently, the best-performing single-stage heat pump is the one that employs the isobutane-propylene mixture.

It is essential to highlight that the compressor simulations relied on a simplified model, where velocity triangles were assumed, and loss correlations were applied. Due to the small size of the compressor impellers, these losses might have been underestimated. Additionally, internal clearance losses and losses in the volute were not considered, which could result in lower isentropic efficiency and COP than the simulations indicated. Moreover, using a centrifugal compressor is worth discussing, as it is based on American Petroleum Institute (API) recommendations that suggest operating a piston compressor at output temperatures no higher than 175 °C. However, maximum output temperatures for this type of compressor are increasing.

In addition to sizing the compressor, the brazed plate HEXs have been sized for the heat pump cycles. A total of three brazed plate HEXs, with a combined effective heat transfer area of 134 m², is required for the single-stage heat pump operating with the isobutane-propylene mixture. The total heat transfer area required when using the butane-hexane mixture is 17.8% smaller; however, this reduction in area is insufficient to offset the significantly lower COP associated with that mixture. For transferring heat between the air and HTFs, a finned tube HEX has been chosen. Since there is no variation in size across the different heat pump cycles, the finned tube HEXs have not been sized.

The best-performing cascade cycle has a COP of 2.68. In this heat pump, the working fluid for the upper cycle consists of 61 mol% isopentane and 39 mol% dimethyl ether, which is operated transcritical. The lower cycle utilises 74 mol% butane and 26 mol% hexane, operating at subcritical conditions. Unlike the optimisation of the single-stage heat pump, the optimisation of the cascade heat pump did not

evaluate all possible molar compositions. Instead, an optimisation logic was employed for each pair in the cascade to determine minimum entropy production. As not every mole fraction was evaluated, it is possible that the identified minimum may not be the absolute lowest but rather a local minimum. Furthermore, only 6.9% of all possible cascade pairs were assessed. The restriction on the temperature range for the working fluid exiting the evaporator of the upper cycle may have also limited the ability to find the optimal cascade heat pump cycle.

A comparison of the COP between the best- and second-best-performing cascade pairs showed only a slight advantage of 0.8% for cascade pair 1, which still outperformed cascade pair 2 when accounting for compressor performance. When comparing the COP of cascade pair 1 to that of the isobutane-propylene single-stage heat pump after adjusting for compressor isentropic efficiency, there is a notable 4.3% advantage for the cascade heat pump. However, it's essential to note that the cascade heat pump requires 91% more heat transfer area and utilises two compressors instead of one. From an economic perspective, the 4.3% increase in COP is likely insufficient to justify the higher capital costs associated with the expanded heat transfer area, and, more importantly, the additional costs of a second compressor.

Considering capital costs, the single-stage heat pump cycle thus demonstrates the best performance. Based on the adjusted COP, the isobutane and propylene mixture outperforms the butane and hexane mixture by 5.1%. Although the butane-hexane mixture requires a lower total heat transfer area, this does not compensate for the performance difference. Therefore, the optimal heat pump cycle for the analysed drying process is a single-stage heat pump using a zeotropic mixture of 96 mol% isobutane and 4 mol% propylene as the working fluid, operating in the transcritical region.

To investigate the impact of the Internal Heat Exchanger (IHX) and the Heat Transfer Fluid (HTF) on the performance of single-stage heat pump cycles, a sensitivity analysis was conducted. The results showed that incorporating an IHX increased the COP by an average of 45.53%. Thus, it can be concluded that the IHX is essential for achieving good performance in a single-stage heat pump. Additionally, removing the HTF cycles resulted in a 5.72% increase in COP. While this is a significant improvement, it is unwise to eliminate the HTF cycles due to the importance of locating the heat pump in a secluded area when using highly flammable or toxic working fluids.

The main research question of this thesis was: *What is the optimal vapour compression heat pump cycle, considering configuration, working fluid selection, and component choice and sizing, for a non-isenthalpic industrial drying process?*

The study demonstrates that the optimal vapour compression heat pump cycle is a single-stage heat pump with an internal heat exchanger that uses a zeotropic mixture consisting of 96 mol% isobutane and 4 mol% propylene as its working fluid, achieving a COP of 2.54. This heat pump features three brazed plate HEXs: a gas cooler with an effective heat transfer area of 95 m², an IHX with an effective area of 16 m², and an evaporator with an effective area of 23 m². The compressor is a two-stage centrifugal compressor operating at 102 krpm, equipped with an impeller having an outer diameter of 61.9 mm in the first stage and 60.1 mm in the second stage.

To compare the results of this study with those of other studies that assume isenthalpic drying, simulations of single-stage heat pumps were conducted with dryer losses ranging from 0% to 30%. The analysis revealed that the COP for the isobutane-propylene mixture increased by 5.87% when isenthalpic drying was assumed, compared with a scenario with 20% dryer losses. Additionally, the sensitivity study indicated that increasing the dryer's dew point to 90 °C increased the COP of the isobutane mixture by 2.92%. When combining isenthalpic drying with a dew point of 90 °C, performance improved further, resulting in a total increase of 11.58% in COP. This significant performance improvement shows that achieving a higher COP requires not just optimising the heat pump cycle but also optimising the dryer.

6

Recommendations

In this study, calculations for the heat exchangers and compressors were conducted only after optimising the heat pumps. For future research on this topic, it is recommended to include the pressure drop across the heat exchangers and to calculate compressor efficiency during the heat pump optimisation process. However, this will demand significantly more computing power, so it's advisable to reduce the parameter space used in this study when integrating pressure drop and efficiency calculations into the optimisation.

Incorporating the pressure drop across the heat exchangers will make the optimised heat pumps more realistic. Additionally, including simulations of the compressor in the optimisation may show that a lower isentropic efficiency leads to a smaller reduction in the COP than this study indicates. This difference arises because, in the compressor simulation, the outlet pressure was set to match the pressure determined during the heat pump optimisation. As the isentropic efficiency decreases, it's possible to achieve the same desired pinch temperature at a lower pressure, which would require less energy input than what the compressor simulations in this study suggest. Therefore, while a lower isentropic efficiency than assumed results in a lower COP, the actual difference may be smaller than the results of this study indicate.

Additionally, considering the power consumption of the fans and pumps required to circulate the air and heat transfer fluids will further improve the realism of heat pump cycle simulations. By accounting for these factors, the heat pump's actual power consumption is taken into account, resulting in a more realistic COP.

Finally, it is recommended to calculate the installed cost of the main components of the proposed heat pumps to assess overall capital expenses. The compressor is likely to be the most expensive component; however, to gain a complete understanding of the total costs, all components should be included in the analysis. This means calculating the costs of the compressors, brazed plate HEXs, and finned-tube HEXs. Understanding these capital costs will allow for the calculation of the payback period, which can help determine whether investing in the heat pump is worthwhile.

References

Alefeld, G. (1987). Efficiency of compressor heat pumps and refrigerators derived from the second law of thermodynamics. *International Journal of Refrigeration*, *10*(6), 331–341. https://doi.org/https://doi.org/10.1016/0140-7007(87)90119-8

API. (2024). Reciprocating compressors for petroleum, chemical, and gas industry services.

Arsenyeva, O., Tovazhnyanskyy, L., Kapustenko, P., Klemeš, J. J., & Varbanov, P. S. (2023). Review of developments in plate heat exchanger heat transfer enhancement for single-phase applications in process industries [Publisher: Multidisciplinary Digital Publishing Institute]. *Energies*, *16*(13), 4976. https://doi.org/10.3390/en16134976

Banuti, D. T. (2015). Crossing the widom-line – supercritical pseudo-boiling. *The Journal of Supercritical Fluids*, *98*, 12–16. https://doi.org/10.1016/j.supflu.2014.12.019

Bell, K. J., & Ghaly, M. A. (1973). An approximate generalized design method for multicomponent partial condenser. *Am. Inst. Chem. Eng. Symp*, 72–79.

Bowman, R. A., Mueller, A. C., & Nagle, W. M. (1940). Mean temperature difference in design. *Transactions of the ASME*, *62*(4), 283–293.

Broerman, E., Manthey, T., Wennemar, J., & Hollingsworth, J. (2019). Chapter 6 - screw compressors. In K. Brun & R. Kurz (Eds.), *Compression machinery for oil and gas* (pp. 253–307). Gulf Professional Publishing. https://doi.org/10.1016/B978-0-12-814683-5.00006-7

Brooks, L. A., Audrieta, L. F., Bluestone, H., & Jofinsox, W. C. (1946). Ammonium carbamate. In *Inorganic syntheses* (pp. 85–86). John Wiley & Sons, Ltd.

Bück, A. (2016). Drying in the chemical industry.

Bücker, D., & Wagner, W. (2006). Reference equations of state for the thermodynamic properties of fluid phase n-butane and isobutane. *Journal of Physical and Chemical Reference Data*, *35*(2), 929–1019. https://doi.org/10.1063/1.1901687

Campbell, J. M. (2014). *Gas conditioning and processing* (R. Hubbard & K. Snow-McGregor, Eds.; 9th Edition, Vol. Volume 2: The Equipment Modules).

Chen, J. C. (1966). Correlation for boiling heat transfer to saturated fluids in convective flow [Publisher: American Chemical Society]. *Industrial & Engineering Chemistry Process Design and Development*, *5*(3), 322–329. https://doi.org/10.1021/i260019a023

Chudnovsky, Y., Buyadgie, O., Buyadgie, D., & Case, E. (2020). *Indirect gas-fired dryer with thermal driven ejector system for bulk food processing*. California Energy Commission. Des Plaines, Illinois. https://www.energy.ca.gov/sites/default/files/2021-05/CEC-500-2020-018.pdf?

Cooper, M. G. (1989). Flow boiling—the 'apparently nucleate' regime. *International Journal of Heat and Mass Transfer*, *32*(3), 459–464. https://doi.org/10.1016/0017-9310(89)90133-6

Coppage, J., & Dallenbach, F. (1956). *Study of supersonic radial compressors for refrigeration and pressurization systems*.

Daily, J. W., & Nece, R. E. (1960). Chamber dimension effects on induced flow and frictional resistance of enclosed rotating disks. *Journal of Basic Engineering*, *82*(1), 217–230. https://doi.org/10.1115/1.3662532

Del Col, D., Cavallini, A., & Thome, J. R. (2005). Condensation of zeotropic mixtures in horizontal tubes: New simplified heat transfer model based on flow regimes. *Journal of Heat Transfer*, *127*(3), 221–230. https://doi.org/10.1115/1.1857951

Dewar, B., Tiainen, J., Jaatinen-Värri, A., Creamer, M., Dotcheva, M., Radulovic, J., & Buick, J. M. (2019). CFD modelling of a centrifugal compressor with experimental validation through radial diffuser static pressure measurement. *International Journal of Rotating Machinery*, *2019*(1). https://doi.org/10.1155/2019/7415263

Dow. (2020). Dowtherm q technical data sheet. https://www.dow.com/en-us/document-viewer.html?docPath=/content/dam/dcc/documents/176/176-01467-01-dowtherm-q-tds.pdf

Eastman. (2021). Technical data sheet therminol® 66 heat transfer fluid. https://productcatalog.eastman.com/tds/ProdDatasheet.aspx?product=71093438&pn=therminol-66-heat-transfer-fluid

ECHA. (2023). *ECHA publishes PFAS restriction proposal*. https://echa.europa.eu/nl/-/echa-publishes-pfas-restriction-proposal

El Hajal, J., Thome, J. R., & Cavallini, A. (2003). Condensation in horizontal tubes, part 1: Two-phase flow pattern map. *International Journal of Heat and Mass Transfer*, *46*(18), 3349–3363. https://doi.org/10.1016/S0017-9310(03)00139-X

El Samad, T., Żabnieńska-Góra, A., Jouhara, H., & Sayma, A. I. (2024). A review of compressors for high temperature heat pumps. *Thermal Science and Engineering Progress*, *51*, 102603. https://doi.org/10.1016/j.tsep.2024.102603

Ganesan, P., Eikevik, T. M., Hamid, K., Wang, R., & Yan, H. (2023). Thermodynamic analysis of cascade high-temperature heat pump using new natural zeotropic refrigerant mixtures: R744/r600 and r744/r601. *International Journal of Refrigeration*, *154*, 215–230. https://doi.org/10.1016/j.ijrefrig.2023.05.017

Gao, K., Wu, J., Bell, I. H., & Lemmon, E. W. (2020). Thermodynamic properties of ammonia for temperatures from the melting line to 725 k and pressures to 1000 MPa, *Journal of Physical and Chemical Reference Data*.

Giampaolo, T. (2023). Compressor types. In *Compressor handbook* (2nd Edition, pp. 15–61). River Publishers. https://doi.org/10.1201/9781003449874

GPSA engineering data book (14th). (2017). Gas Processors Association.

Heinrich, M. (2016). *Genetic optimization of turbomachinery components using the volute of a transonic centrifugal compressor as a case study* [Doctoral dissertation, Technische Universität Bergakademie Freiberg].

Hewitt, G. F., Shires, G. L., & Bott, T. R. (1994). *Process heat transfer*. CRC Press.

Hoang, D. K., Walmsley, T. G., Cleland, D. J., Chen, Q., & Carson, J. K. (2025). Thermo-economic investigation and multi objective optimization of cascade high temperature heat pump using low global warming refrigerants. *Applied Thermal Engineering*, *279*, 127901. https://doi.org/10.1016/j.applthermaleng.2025.127901

Hollingsworth, J., Phillippi, G., Hinchliff, M., Kulhanek, C., Rimpel, A. M., & Maywald, F. (2019). Chapter 5 - reciprocating compressors. In K. Brun & R. Kurz (Eds.), *Compression machinery for oil and gas* (pp. 167–252). Gulf Professional Publishing. https://doi.org/10.1016/B978-0-12-814683-5.00005-5

Huang, X., Zhang, J., & Haglind, F. (2025). An experimental study of flow boiling heat transfer and pressure drop of hydrofluoroolefin and hydrocarbon mixtures in a plate heat exchanger. *International Journal of Thermal Sciences*, *212*, 109762. https://doi.org/10.1016/j.ijthermalsci.2025.109762

Huang, Y., Li, G., Tang, X., Huang, K., Zhao, W., & Zhang, J. (2025). Thermodynamic analysis of a modified cascade high temperature heat pump with zeotropic mixtures for heating production up to 200 °c. *Energy Conversion and Management*, *324*, 119307. https://doi.org/10.1016/j.enconman.2024.119307

Hundy, G. F., Trott, A. R., & Welch, T. C. (2016). Chapter 8 - expansion valves. In G. F. Hundy, A. R. Trott, & T. C. Welch (Eds.), *Refrigeration, air conditioning and heat pumps (fifth edition)* (pp. 135–146). Butterworth-Heinemann. https://doi.org/10.1016/B978-0-08-100647-4.00008-5

IEA. (2007). *Tracking industrial energy efficiency and CO2 emissions*. IEA. Paris. https://www.iea.org/reports/tracking-industrial-energy-efficiency-and-co2-emissions

IEA. (2023). *Tracking clean energy progress 2023*. IEA. Paris. https://www.iea.org/reports/tracking-clean-energy-progress-2023

Incropera, F., & Dewitt, D. P. (1996). *Introduction to heat transfer*. John Wiley&Sons.

Jansen, W. (1967). A method for calculating the flow in a centrifugal compressor when entropy gradient are present, 133–146.

Japiske, D. (1982). Advanced diffusion levels in turbocharger compressors and component matching, 143.

Japiske, D. (1996). *Centrifugal compressor design and performance*.

Jesper, M., Schlosser, F., Pag, F., Walmsley, T. G., Schmitt, B., & Vajen, K. (2021). Large-scale heat pumps: Uptake and performance modelling of market-available devices. *Renewable and Sustainable Energy Reviews*, *137*, 110646. https://doi.org/10.1016/j.rser.2020.110646

Johnston, J. P., & Dean, R. C., Jr. (1966). Losses in vaneless diffusers of centrifugal compressors and pumps: Analysis, experiment, and design. *Journal of Engineering for Power*, *88*(1), 49–60. https://doi.org/10.1115/1.3678477

Kiss, A. A., & Infante Ferreira, C. A. (2016). *Heat pumps in chemical process industry*. CRC Press. https://doi.org/10.1201/9781315371030

Kubba, S. (2017). Impact of energy and atmosphere. In *Handbook of green building design and construction* (pp. 443–571). Elsevier. https://doi.org/10.1016/B978-0-12-810433-0.00009-5

Kus, B., & Nekså, P. (2013). Development of one-dimensional model for initial design and evaluation of oil-free co2 turbo-compressor. *International Journal of Refrigeration*, *36*(8), 2079–2090. https://doi.org/10.1016/j.ijrefrig.2013.05.009

Lazzarin, R., & Noro, M. (2008). Experimental comparison of electronic and thermostatic expansion valves performances in an air conditioning plant. *International Journal of Refrigeration*, *31*(1), 113–118. https://doi.org/10.1016/j.ijrefrig.2007.09.004

Lemmon, E. W., Bell, I. H., Huber, M. L., & McLinden, M. O. (2018). NIST standard reference database 23: Reference fluid thermodynamic and transport properties-REFPROP, version 10.0, national institute of standards and technology. https://www.nist.gov/srd/refprop

Lemmon, E. W., Mclinden, M. O., Overhoff, U., & Wagner, W. (2018). A reference equation of state for propylene for temperatures from the melting line to 575 k and pressures up to 1000 MPa. *to be submitted to Journal of Physical and Chemical Reference Data*.

Lemmon, E. W., McLinden, M. O., & Wagner, W. (2009). Thermodynamic properties of propane. III. a reference equation of state for temperatures from the melting line to 650 k and pressures up to 1000 MPa [Last Modified: 2021-06-02T18:30-04:00 Publisher: Eric W. Lemmon, Mark O. McLinden, W Wagner]. *NIST*, *54*, 3141–3180. Retrieved July 15, 2025, from https://www.nist.gov/publications/thermodynamic-properties-propane-iii-reference-equation-state-temperatures-melting-line

Lemmon, E. W., & Span, R. (2006). Short fundamental equations of state for 20 industrial fluids [Publisher: American Chemical Society]. *Journal of Chemical & Engineering Data*, *51*(3), 785–850. https://doi.org/10.1021/je050186n

Logie, J., Tran, M. C., & Vanslambrouck, B. (2016). DEVELOPMENT OF a DYNAMIC HEAT PUMP DRYER TEST BENCH TO DEMONSTRATE ENERGETICAL OPTIMIZATION POSSIBILITIES BY REPLICATING REAL LIFE DRYING PROCESSES. *The 20th International Drying Symposium*.

Lorenz, H. (1895). Die ermittelung der grenzwerte der thermodynamischen energieumwandlung. *Zeitschrift für die gesammte Kälte-Industrie*, (2), 6–12.

Lu, K., Sultan, I. A., & Phung, T. H. (2023). A literature review of the positive displacement compressor: Current challenges and future opportunities [Number: 20 Publisher: Multidisciplinary Digital Publishing Institute]. *Energies*, *16*(20), 7035. https://doi.org/10.3390/en16207035

Marina, A., Spoelstra, S., Zondag, H. A., & Wemmers, A. K. (2021). An estimation of the european industrial heat pump market potential. *Renewable and Sustainable Energy Reviews*, *139*. https://doi.org/10.1016/j.rser.2020.110545

Martin, H. (1996). A theoretical approach to predict the performance of chevron-type plate heat exchangers. *Chemical Engineering and Processing: Process Intensification*, *35*(4), 301–310. https://doi.org/10.1016/0255-2701(95)04129-X

Montreal protocol on substances that deplete the ozone layer final act 1987. (1989). *Journal of Environmental Law*, *1*(1), 128–136. https://doi.org/10.1093/jel/1.1.128

Mujumdar, A. S. (2007). Principles, classification, and selection of dryers. In A. S. Mujumdar (Ed.), *Handbook of industrial drying* (third edition). CRC Press.

Naukkarinen, T. (2013). *The aerodynamic design of a centrifugal compressor* [Doctoral dissertation, Lappeenranta University of Technology].

Ni, H., Hu, P., & Li, Y. (2025). Analysis and optimization of the performance of closed heat pump dryer based on zeotropic mixtures. *Applied Thermal Engineering*, *260*, 124916. https://doi.org/10.1016/j.applthermaleng.2024.124916

Ogunedo, B. M. O. (2020, January 1). Chapter 11 - effects of fouling. In L. Pekař (Ed.), *Advanced analytic and control techniques for thermal systems with heat exchangers* (pp. 247–259). Academic Press. https://doi.org/10.1016/B978-0-12-819422-5.00011-6

Oh, H.-W. (1999). *Investigation on the design and performance analysis methods of centrifugal turbomachines* [Doctoral dissertation, KAIST] [Accepted: 2011-12-14T05:17:05Z Publisher: □□□□□□□]. Retrieved September 29, 2025, from https://koasas.kaist.ac.kr/handle/10203/42956

Peters, M. S., Timmerhaus, K. D., & West, R. E. (2003). *Plant design and economics for chemical engineers* (Vol. 4). McGraw-Hill New York.

Roetzel, W., & Spang, B. (2010). C3 - typical values of overall heat transfer coefficients. In VDI-GVC (Ed.), *VDI heat atlas* (2nd Edition). Springer.

Setzmann, U., & Wagner, W. (1991). A new equation of state and tables of thermodynamic properties for methane covering the range from the melting line to 625 k at pressures up to 1000 MPa. *Journal of Physical and Chemical Reference Data*, *20*(6), 1061–1155. https://doi.org/10.1063/1.555898

Sharevska, M., Sharevska, M., Brem, G., Hoogsteen, G., Hurink, J., Pozarlik, A., & Hajimolana, Y. (2025). Comprehensive study of high temperature heat pump configurations: A framework of performance and application. *Energy*, *334*, 137525. https://doi.org/10.1016/j.energy.2025.137525

Smith, R. (2016). Chapter 13 - pumping and compression. In *Chemical process design and integration* (Second edition, pp. 349–375). John Wiley & Sons, Inc.

Smukala, J., Span, R., & Wagner, W. (2000). New equation of state for ethylene covering the fluid region for temperatures from the melting line to 450 k at pressures up to 300 MPa. *Journal of Physical and Chemical Reference Data*, *29*(5), 1053–1121. https://doi.org/10.1063/1.1329318

Span, R., & Wagner, W. (1996). A new equation of state for carbon dioxide covering the fluid region from the triple□point temperature to 1100 k at pressures up to 800 MPa. *Journal of Physical and Chemical Reference Data*, *25*(6), 1509–1596. https://doi.org/10.1063/1.555991

Stoecker, W. F. (1998). 12.11 - compatibility with the material refrigerants contact. In *Industrial refrigeration handbook*.

Taborek, J. (1994). Charts for mean temperature difference in industrial heat exchanger configurations [ed. G. F. Hewitt]. In *Heat exchanger design handbook*. Begell House.

Tao, X., & Infante Ferreira, C. A. (2019). Heat transfer and frictional pressure drop during condensation in plate heat exchangers: Assessment of correlations and a new method. *International Journal of Heat and Mass Transfer*, *135*, 996–1012. https://doi.org/10.1016/j.ijheatmasstransfer.2019.01.132

Thol, M., Uhde, T., Lemmon, E. W., & Span, R. (2018a). Fundamental equations of state for hydrocarbons. part i. n-pentane. *to be published*.

Thol, M., Uhde, T., Lemmon, E. W., & Span, R. (2018b). Fundamental equations of state for hydrocarbons. part II. n-hexane. *to be published*.

Thome, J. R., El Hajal, J., & Cavallini, A. (2003). Condensation in horizontal tubes, part 2: New heat transfer model based on flow regimes. *International Journal of Heat and Mass Transfer*, *46*(18), 3365–3387. https://doi.org/10.1016/S0017-9310(03)00140-6

Thome, J. R. (1996). Boiling of new refrigerants: A state-of-the-art review. *International Journal of Refrigeration*, *19*(7), 435–457. https://doi.org/10.1016/S0140-7007(96)00004-7

Tijani, M. E. H., Otero Rodriguez, G. J., Ramirez, M., Poulsen, J. L., & Spoelstra, S. (2025). Selection of lubricant oils for high temperature heat pumps: A review and selection methodology guidelines. *Applied Thermal Engineering*, *273*, 126483. https://doi.org/10.1016/j.applthermaleng.2025.126483

Underwood, J. V. (1934). The calculation of the mean temperature difference in multipass heat exchangers. *Institution of Petroleum Technologists*, *20*, 145–158.

United Nations. (n.d.). *For a livable climate: Net-zero commitments must be backed by credible action* [United nations | climate action] [Publisher: United Nations]. Retrieved April 3, 2025, from https://www.un.org/en/climatechange/net-zero-coalition

Uusitalo, A., Jaatinen-Värri, A., Turunen-Saaresti, T., Honkatukia, J., & Tiainen, J. (2024). Centrifugal compressor design and cycle analysis of large-scale high temperature heat pumps using hydrocarbons. *Applied Thermal Engineering*, *247*, 123035. https://doi.org/10.1016/j.applthermaleng.2024.123035

Uusitalo, A., Turunen-Saaresti, T., Honkatukia, J., Tiainen, J., & Jaatinen-Värri, A. (2020). Numerical analysis of working fluids for large scale centrifugal compressor driven cascade heat pumps upgrading waste heat. *Applied Energy*, *269*, 115056. https://doi.org/10.1016/j.apenergy.2020.115056

Vieren, E., Demeester, T., Beyne, W., Arteconi, A., De Paepe, M., & Lecompte, S. (2023). The thermodynamic potential of high-temperature transcritical heat pump cycles for industrial processes with large temperature glides. *Applied Thermal Engineering*, *234*, 121197. https://doi.org/10.1016/j.applthermaleng.2023.121197

Wang, P., Kowalski, S., Sun, J., Gao, Z., Yang, C.-M., & Nawaz, K. (2024). Technology feasibility of high-temperature heat pumps for industrial drying process in the US. *International Refrigeration and Air Conditioning Conference*, *2527*, 1–10. https://docs.lib.purdue.edu/iracc/2527/

Wennemar, J. (2009). Dry screw compressor performance and application range. *The thirty-eight turbomachinery symposium*.

Widdows, P. I. (2024). *Heat pump for industrial drying processes* [Master thesis]. TU Delft.

Wu, J., Zhou, Y., & Lemmon, E. W. (2011). An equation of state for the thermodynamic properties of dimethyl ether [Publisher: AIP Publishing]. *Journal of Physical and Chemical Reference Data*, *40*(2). https://doi.org/10.1063/1.3582533

Yan, Y.-Y., & Lin, T.-F. (1999). Evaporation heat transfer and pressure drop of refrigerant r-134a in a plate heat exchanger. *Journal of Heat Transfer*, *121*(1), 118–127. https://doi.org/10.1115/1.2825924

Zendehboudi, A., Ye, Z., Hafner, A., Andresen, T., & Skaugen, G. (2021). Heat transfer and pressure drop of supercritical CO2 in brazed plate heat exchangers of the tri-partite gas cooler. *International Journal of Heat and Mass Transfer*, *178*, 121641. https://doi.org/10.1016/j.ijheatmasstransfer.2021.121641

Zhang, J., Elmegaard, B., & Haglind, F. (2021a). Condensation heat transfer and pressure drop characteristics of zeotropic mixtures of r134a/r245fa in plate heat exchangers. *International Journal of Heat and Mass Transfer*, *164*, 120577. https://doi.org/10.1016/j.ijheatmasstransfer.2020.120577

Zhang, J., Elmegaard, B., & Haglind, F. (2021b). Condensation heat transfer and pressure drop correlations in plate heat exchangers for heat pump and organic rankine cycle systems. *Applied Thermal Engineering*, *183*, 116231. https://doi.org/10.1016/j.applthermaleng.2020.116231

Zhang, J., & Haglind, F. (2021). Experimental analysis of high temperature flow boiling heat transfer and pressure drop in a plate heat exchanger. *Applied Thermal Engineering*, *196*, 117269. https://doi.org/10.1016/j.applthermaleng.2021.117269

Zhao, A., Pecnik, R., & Peeters, J. W. (2024). Thermodynamic analysis and heat exchanger calculations of transcritical high-temperature heat pumps. *Energy Conversion and Management*, *303*, 118172. https://doi.org/10.1016/j.enconman.2024.118172

Zhu, X., & Haglind, F. (2020). Computational fluid dynamics modeling of liquid–gas flow patterns and hydraulics in the cross-corrugated channel of a plate heat exchanger. *International Journal of Multiphase Flow*, *122*, 103163. https://doi.org/10.1016/j.ijmultiphaseflow.2019.103163

Zühlsdorf, B. (2023). *High -temperature heat pumps, annex 58*. Heat Pump Center. Borås, Sweden.

Zühlsdorf, B., Jensen, J. K., Cignitti, S., Madsen, C., & Elmegaard, B. (2018). Analysis of temperature glide matching of heat pumps with zeotropic working fluid mixtures for different temperature glides. *Energy*, *153*, 650–660. https://doi.org/10.1016/j.energy.2018.04.048

A Code structure single-stage heat pump

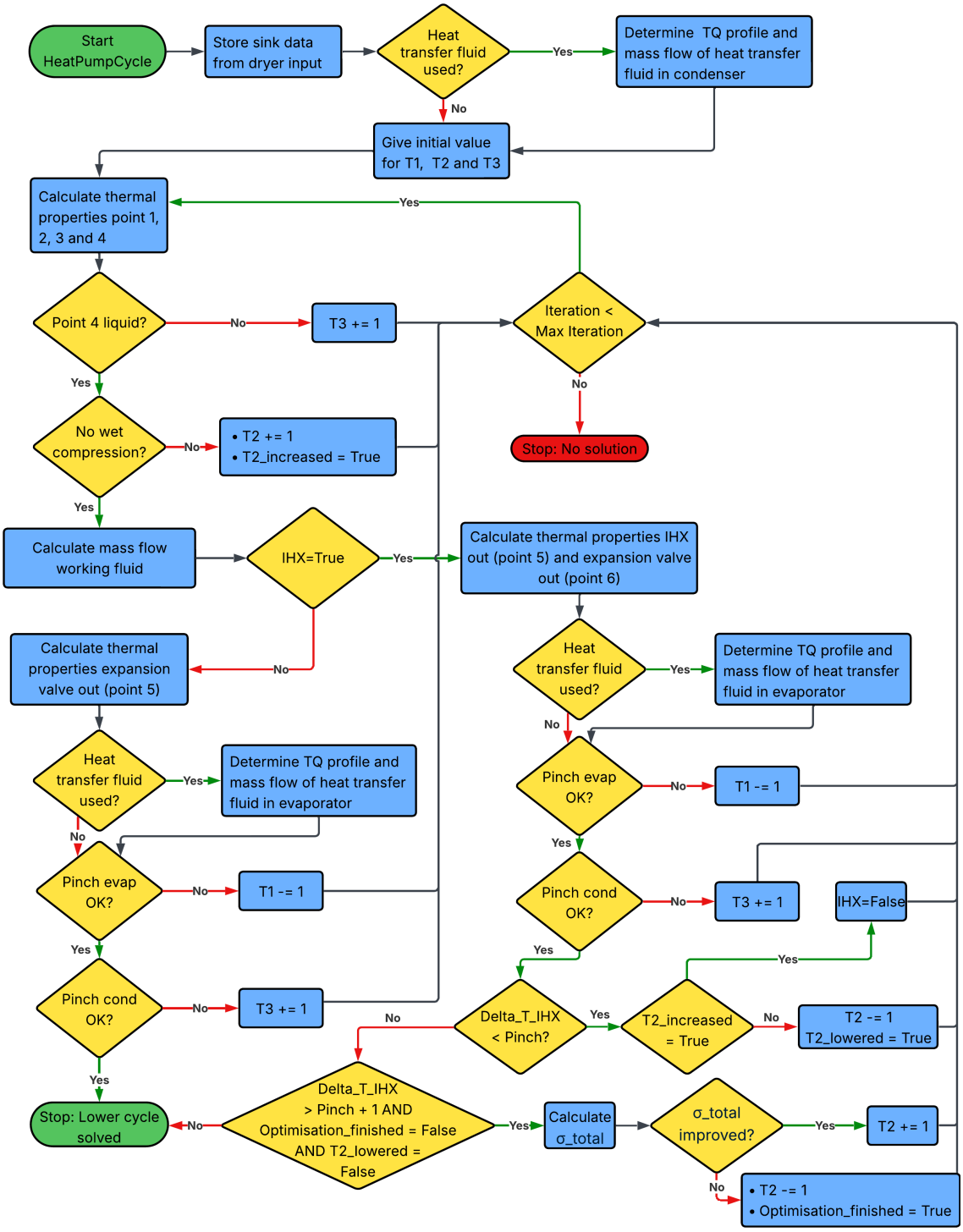

Figure A.1: Flowchart of the simulation of the single-stage heat pump.

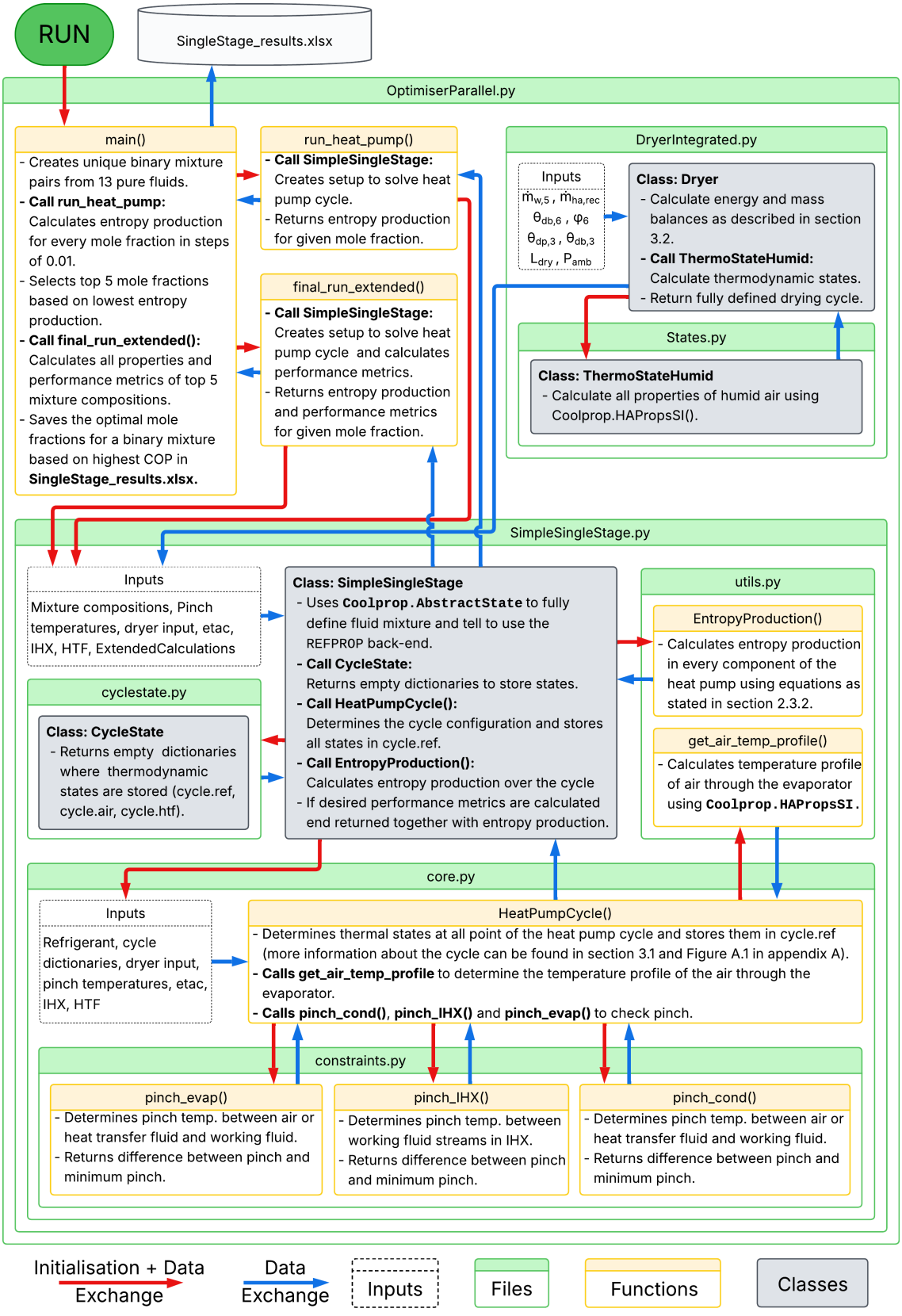

Figure A.2: Code structure for the single-stage heat pump optimisation and simulation.

B Code structure cascade heat pump

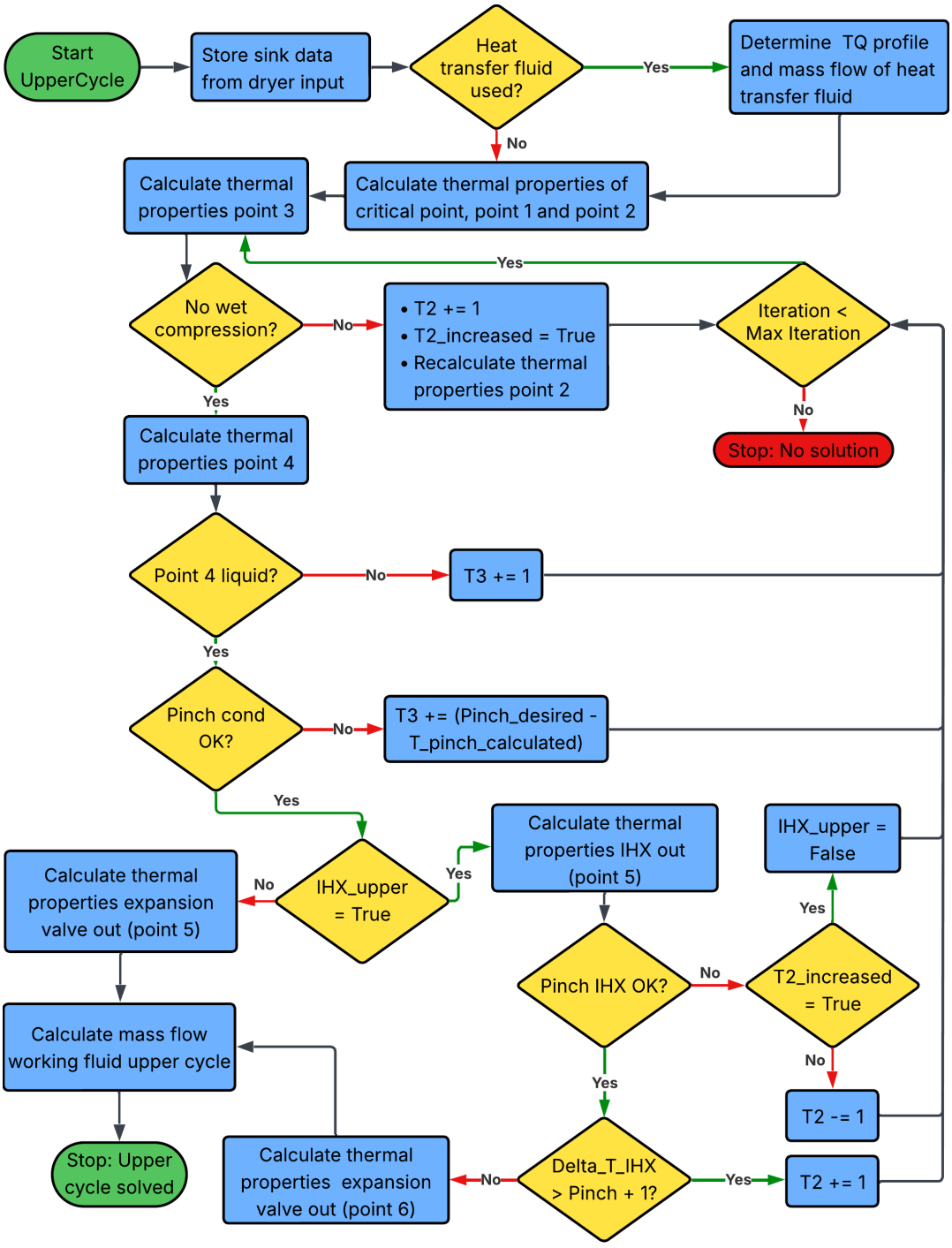

Figure B.1: Flow chart of the simulation of the upper cycle in the cascade heat pump.

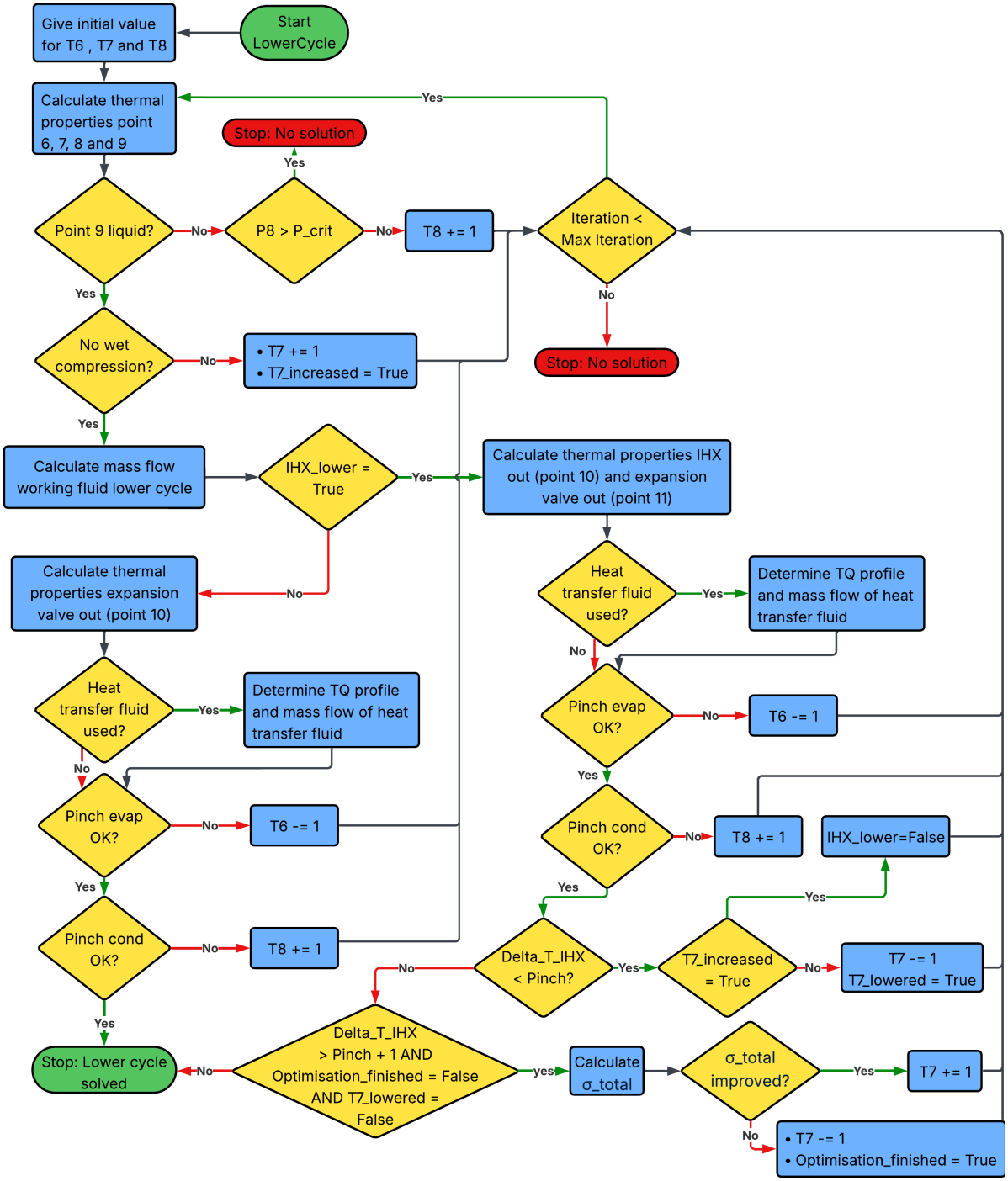

Figure B.2: Flow chart of the simulation of the lower cycle in the cascade heat pump.

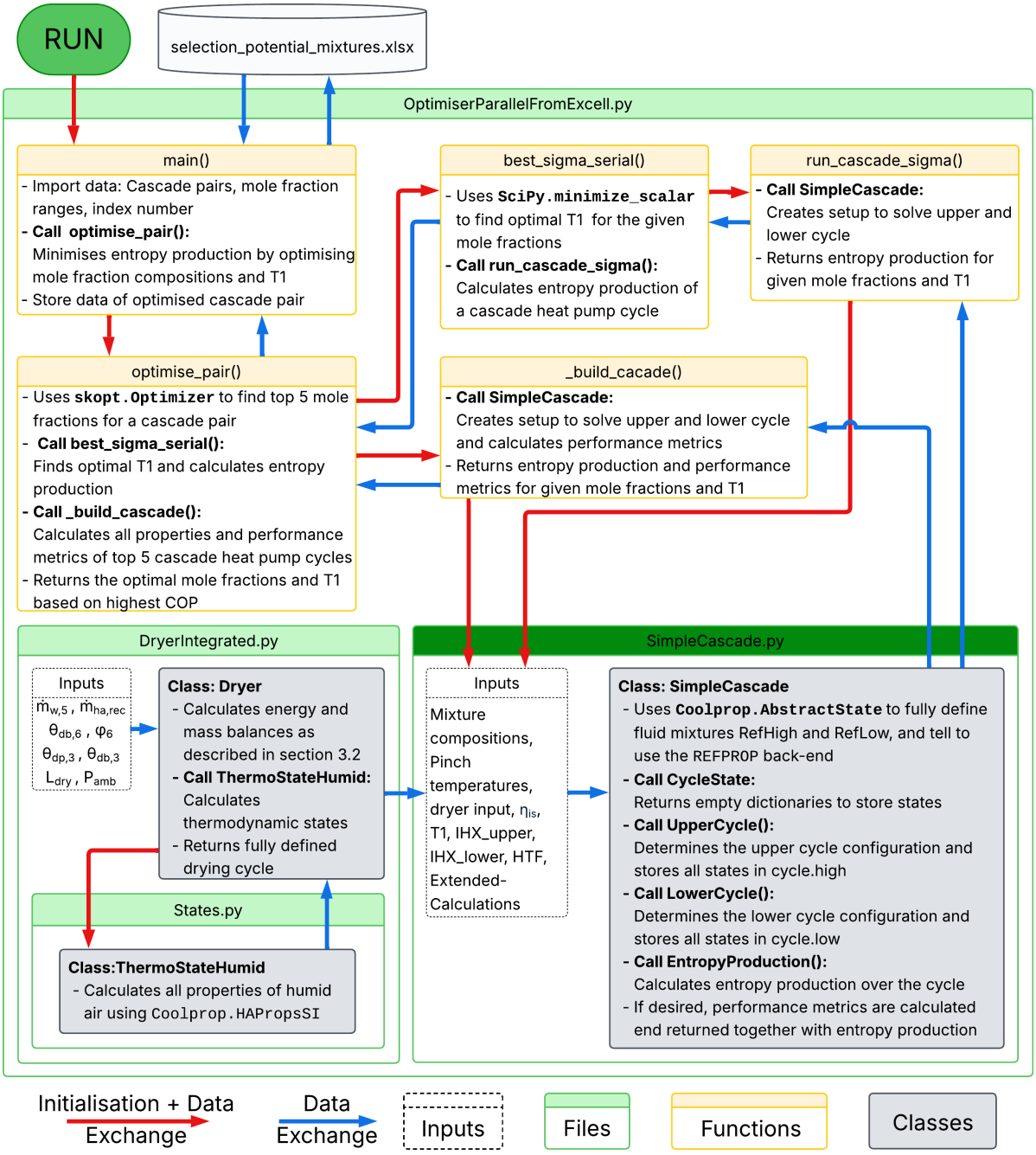

Figure B.3: Code structure without details on SimpleCascade class (see for a more detailed SimpleCascade class Figure B.4).

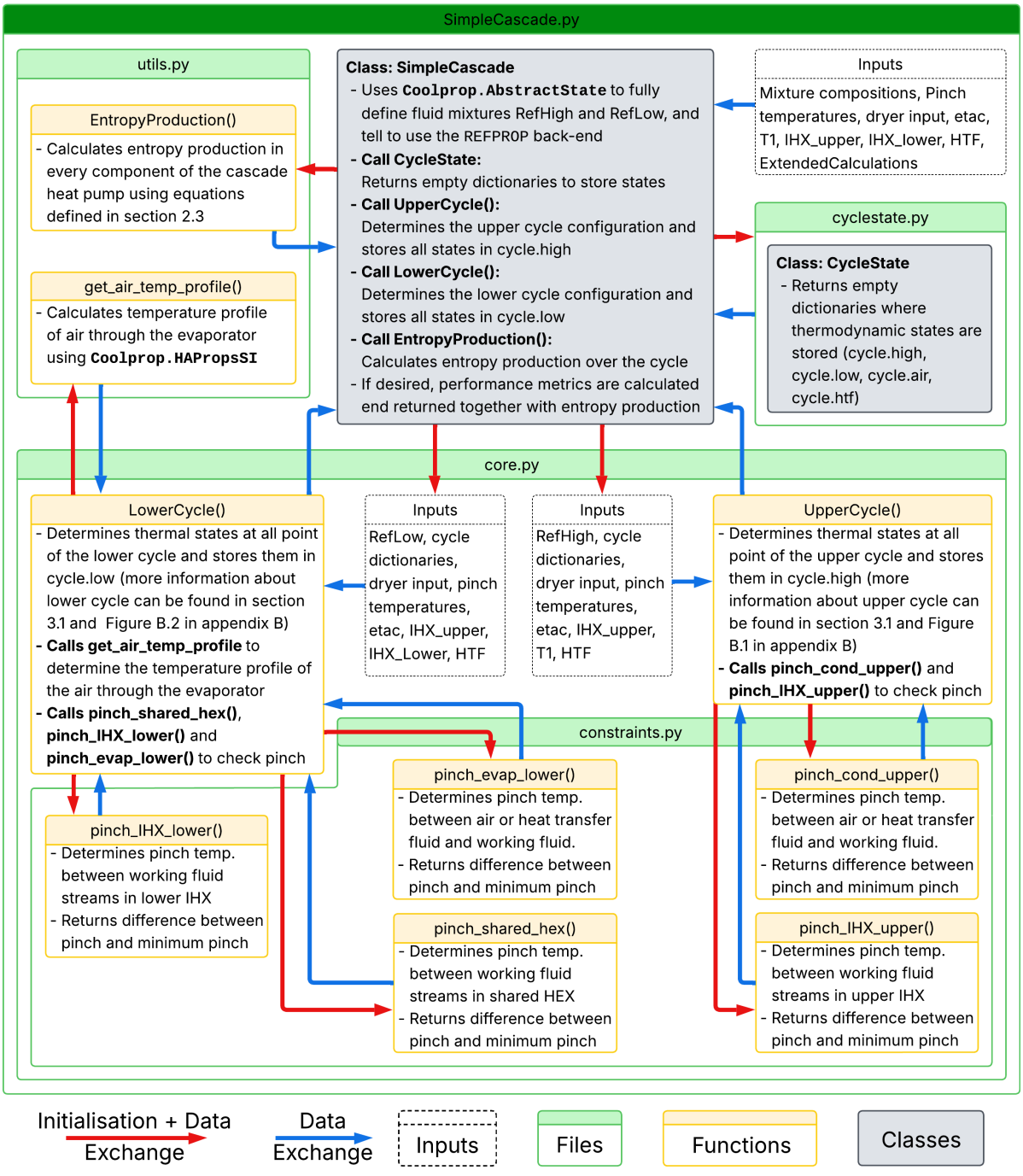

Figure B.4: Code structure zoomed in on SimpleCascade.py.